Journal of Fluids and Structures 127 (2024) 104122

Contents lists available at ScienceDirect

Journal of Fluids and Structures

journal homepage: www.elsevier.com/locate/jfs

Spatio-temporal relationship between three-dimensional deformations of a collapsible tube and the downstream flowfield

Vikas N. Bhargav [a,*], Nicola Francescato [a,b], Holger Mettelsiefen [a], Abdullah Y. Usmani [a], Stefania Scarsoglio [b], Vrishank Raghav [a,*]

[a] Auburn University, Department of Aerospace Engineering, Auburn, 36849, AL, USA
[b] Politecnico di Torino, Department of Mechanical and Aerospace Engineering, Turin, 10129, Italy

ARTICLE INFO

Keywords:
Compliant tube
Stereo-photogrammetry
Planar PIV
Surface deformations
Shear stress

ABSTRACT

The interactions between fluid flow and structural components of collapsible tubes are representative of those in several physiological systems. Although extensively studied, there exists a lack of characterization of the three-dimensionality in the structural deformations of the tube and its influence on the flow field. This experimental study investigates the spatio-temporal relationship between 3D tube geometry and the downstream flow field under conditions of fully open, closed, and slamming-type oscillating regimes. A methodology is implemented to simultaneously measure three-dimensional surface deformations in a collapsible tube and the corresponding downstream flow field. Stereophotogrammetry was used to measure tube deformations, and simultaneous flow field measurements included pressure and planar Particle Image Velocimetry (PIV) data downstream of the collapsible tube. The results indicate that the location of the largest collapse in the tube occurs close to the downstream end. In the oscillating regime, sections of the tube downstream of the largest mean collapse experience the largest oscillations in the entire tube that are completely coherent and in phase. At a certain streamwise distance upstream of the largest collapse, a switch in the direction of oscillations occurs with respect to those downstream. Physically, when the tube experiences constriction downstream of the location of the largest mean collapse, this causes the accumulation of fluid and build-up of pressure in the upstream regions and an expansion of these sections. Fluctuations in the downstream flow field are significantly influenced by tube fluctuations along the minor axes. The fluctuations in the downstream flowfield are influenced by the propagation of disturbances due to oscillations in tube geometry, through the advection of fluid through the tube. Further, the manifestation of the LU-type pressure fluctuations is found to be due to the variation in the propagation speed of the disturbances during the different stages within a period of oscillation of the tube.

1. Introduction

The dynamics of collapsible tubes draws inspiration from several phenomena observed in biological systems (Grotberg and Jensen, 2004; Bai and Zhu, 2019). For instance in the respiratory system, constricted airways in asthma patients limit air expulsion from the lungs, leading to wheezing (Bertram and Elliott, 2003). Collapse of the upper airways can also be relevant to obstructive sleep apnea (Amin et al., 2021) and snoring (Bertram, 2008). In the cardiovascular system, the potential collapse of the coronary

* Corresponding authors.
E-mail addresses: vnb0008@auburn.edu (V.N. Bhargav), raghav@auburn.edu (V. Raghav).

https://doi.org/10.1016/j.jfluidstructs.2024.104122
Received 15 October 2023; Received in revised form 2 April 2024; Accepted 8 April 2024
Available online 24 April 2024

arteries occurs due to heart contraction. Furthermore, sphygmomanometry produces 'Korotkoff sounds' due to flow-induced vibration in brachial arteries (Bertram et al., 1989). During muscular compression, veins collapse while pumping blood against gravity or in the event of therapeutic compression in deep-vein thrombosis treatment (Dai et al., 1999). Additionally, collapsible tubes also find relevance in engineering applications such as oil transport, the pharmaceutical and cosmetic industry (Kumar and Prabhakaran, 2022). These applications relate to Fluid–Structure Interactions (FSI), whose modeling is quite challenging due to the existence of large-scale deformations, flow three-dimensionality, and low Reynolds number turbulence, which have attracted many researchers in the past decades.

A simplified approach to studying collapsible tubes is the Starling resistor model (Knowlton and Starling, 1912). It is a classical bench-top experimental model where the compliant tube is enclosed in a pressurized chamber and is secured to rigid tubes at its inlet and outlet. Tube thickness and transmural pressure are two important factors that affect tube collapse. These are governed by the tube law (Shapiro, 1977) that relates the transmural pressure, $\Delta p_{\mathrm{tr}} = p_{\mathrm{ex}} - p_{\mathrm{dn}}$ to the cross-sectional area, where p_{dn} is the internal pressure and p_{ex} is the external pressure. For $\Delta p_{\mathrm{tr}} < 0$, the tube attains a circular cross section, while at a sufficiently large positive value of $\Delta p_{\mathrm{tr}} > 0$ the tube deforms to an elliptical shape. Under limiting conditions, the walls touch each other to acquire a dumbbell shape having two lobes establishing a flow-limiting configuration. Furthermore, when $\Delta p_{\mathrm{tr}} \sim 0$, the compliance of the tube increases and small pressure fluctuations within the flow generate large changes in the area. An interesting feature of this system is that for a particular positive threshold value of Δp_{tr}, self-excited oscillations are induced in the tube, which manifest themselves in the form of flow field fluctuations.

Several simplified theoretical and numerical models have been developed in the past to investigate self-excited oscillations in the Starling resistor. The earliest theoretical models were lumped-parameter models (Conrad, 1969; Bertram and Pedley, 1982) that describe the behavior of the system through a few variables, i.e., cross-sectional area, transmural pressure, and flow velocity at the point of collapse; however, they failed to capture the wave propagation. Then, 1D models (Katz et al., 1969; Shapiro, 1977; Jensen, 1990; Cancelli and Pedley, 1985) provided useful estimates of the bulk flow, but all flow features could not yet be fully resolved. They relied on several *ad hoc* assumptions while incorporating the effect of viscous losses and flow separation, which were shown to be incorrect (Luo and Pedley, 1996). The 2D model (Pedley, 1992) was then introduced, consisting of a planar channel with a portion of one of the walls being replaced by a flexible membrane under tension. Following this, several aspects of this model have been addressed in the literature (Luo and Pedley, 1995, 1998, 2000; Jensen and Heil, 2003; Liu et al., 2009; Tang et al., 2015). Further, these models have been extended to 3D modeling (Hazel and Heil, 2003; Marzo et al., 2005; Sen et al., 2018), and have been helpful in comparing them with experiments (Bertram et al., 1990; Wang et al., 2009).

Heil and Hazel (2011) provides a comprehensive discussion of earlier experimental studies, and henceforth a subset of them is discussed. Bertram and Elliott (2003) focused on visualizing the flow field and self-excited oscillations by varying the flow rate and transmural pressure. Bertram et al. (1990) reported that for particular LU-type oscillations (L - frequency, low; up) the collapsed tube resembling a two-lobed cross-section established two jet-like structures along the tube's major axis that impinge on the wall at a downstream location creating two sickle-shaped regions of increased axial velocity. These flow features were evident for laminar flows at $Re \approx 300$ (Bertram et al., 2008) and turbulent flows at $Re \approx 10{,}000$ (Bertram and Nugent, 2005) at low oscillation frequency. However, for sufficiently thin-walled tubes, self-excited LU-type oscillations developed at $Re \approx 300$, with a maximum frequency of 10 Hz. On the basis of the experimental data, 3D FSI modeling helped in understanding the self-excitation phenomenon, while 1D and 2D models only gave information about the key flow features. Recent experimental studies have also been reported. Wu et al. (2015) measured the evolution of a cross section of the tube by employing oblique high-speed imaging and identified two self-excited periodic states and one transitional oscillation state. Wall oscillations in collapsible tubes have been addressed while considering steady Newtonian shear-thinning fluids (Nahar et al., 2019) and pulsatile (Stelios et al., 2019) internal flow as well. Anderson et al. (2016) established experiments of a 2D collapsible channel to validate the FSI simulations. Podoprosvetova et al. (2021) explored the stability and oscillation dynamics of collapsible tubes under laminar and turbulent conditions. Kumar and Prabhakaran (2022) reported the effect of unsteady external pressure on tube oscillations.

The above studies involved tracking the streamwise tube cross section about the primary axis of collapse, while also capturing the velocity field inside the tube. Furthermore, they performed two-dimensional measurements of tube geometry at specific cross sections along the tube length. Although these studies did not disregard the three-dimensionality of the tube under collapse, the simultaneous measurements of two-dimensional cross-sections at different locations on the tube are still lacking. This significantly limits our understanding of the dynamics of the tube under self-excited oscillations. Finally, the influence of three-dimensionality in the tube collapse on the downstream flow field begs attention, especially under self-excited oscillations as it is expected to have physiological implications. In particular, in cardiovascular flows, the mean and fluctuating components of shear stress exerted on the walls of the arteries and blood vessels are known to promote the growth of abnormalities and lead to rupture. Therefore, the objectives of this study are as follows:

1. Implement a methodology to simultaneously measure the three dimensional surface deformations in a collapsible tube and the corresponding downstream flow field.
2. Investigate the fluid–structure interaction physics and spatio-temporal relationship between the three-dimensionality in collapsible tube deformations and the downstream flow field.

This approach to the measurement of the tube geometry is expected to provide an invaluable validation dataset for future modeling and numerical studies, and to glean new physical insights, owing to the rich temporal and spatial resolution. Further, this technique will also be useful to accurately study the deformations in scaled geometric models of physiological flows, to predict biomedical implications *ex-vivo*.

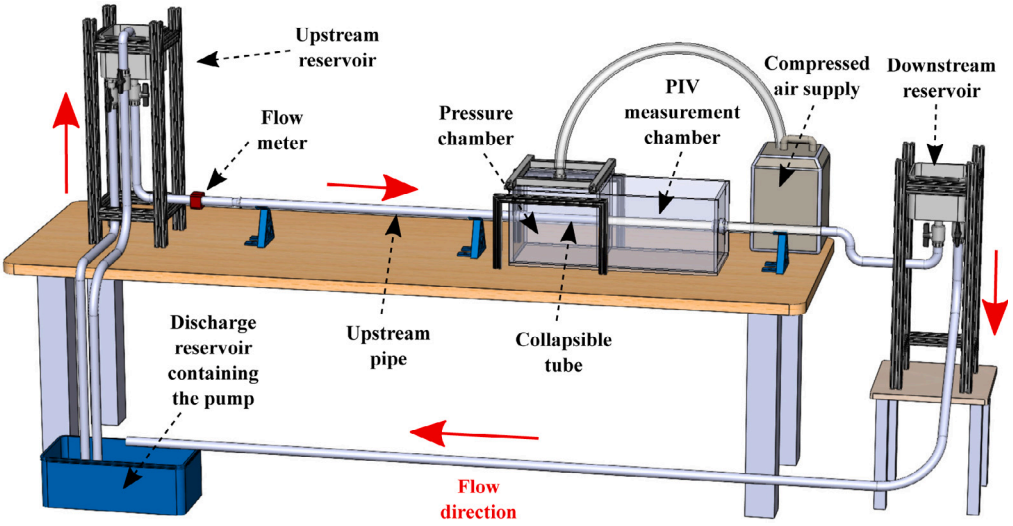

Fig. 1. Schematic of flow loop.

2. Methods

2.1. Experimental setup

The experiments were conducted at Auburn University using a setup that consisted of a flow loop as shown in Fig. 1. A submersible centrifugal pump (Active Aqua AAPW1000), placed in a large discharge reservoir of the working fluid maintained the fluid flow through the system. A 70–30 glycerin–water mixture by volume was used during the experiments. The outlet of the pump delivered the fluid to a raised upstream reservoir with two outlets. One of the outlets was attached to a valve that controlled the flow rate through the collapsible tube. The other outlet in the reservoir drained the excess fluid in the scenario when the valve closure was significant, such that the head remained constant throughout the experiments. The outlet of the valve was connected to a flow straightener and a rigid horizontal acrylic tube in series. The tube had a circular profile with an internal diameter (D) of 25.4 mm, and a length of 40D. The collapsible tube with the same internal diameter was attached to the end of the rigid tube and held in place inside an acrylic pressure chamber with optical access for stereophotogrammetry. This chamber was partially filled with a glycerin–water mixture such that it completely submerged the collapsible tube while also leaving some room for air. Keeping the tube immersed in the fluid helped prevent it from sagging due to its own weight and maintained uniform hydro-static pressure. It was critical not to completely fill the pressure chamber with a liquid because it could suppress self-sustained oscillations in the tube. A compressed air supply from the building was used to maintain the required pressure (up to 8 kPa) within this chamber through a suitable valve. This supply was provided through a pressure reservoir/compliance chamber to extend the air volume so that the pressure variations remained small over time. The collapsible tube was connected to another rigid acrylic tube of length 30D downstream. This tube, which enabled measurement of the velocity field, was also placed inside another adjacent acrylic chamber. This chamber was also filled with a glycerin–water mixture, which submerged the acrylic tube. The refractive index of commercially available acrylic sheets are in the range of 1.489–1.490. The refractive index of the glycerin–water solution used in our study is 1.428–1.432, as measured with a refractometer. The resulting ratio of refractive indices is between 1.036 and 1.044. This helped reduce the mismatch in the refractive index between the acrylic tube and working fluid inside it and outside, thereby reducing optical distortions. The outlet of this tube was connected to another flow control valve, which in turn drained into a downstream reservoir. The heights of both the upstream and downstream reservoirs could be adjusted in addition to the flow control valves, to achieve precise flow rates. Finally, the downstream reservoir drained the fluid to the discharge reservoir that contains the pump.

2.2. Tube design and characterization

Three parameters were known to play a critical role in influencing fluid–structure interactions in a collapsible tube. These were the ratio of tube length to internal diameter (L/D), the ratio of tube thickness to internal diameter (t_t/D), and the tube stiffness parameter (K_s). Firstly, for tubes with large L/D values, the weight of the tube might cause sagging. But for smaller L/D values, the tension in the tube was expected to play a dominant role. Therefore, the tube dimensions had to be chosen considering a compromise between the two effects. Secondly, a large t_t/D value would increase the stiffness of the tube and could make it non-compliant. Therefore, the tube thickness also had to be optimally chosen. The stiffness parameter K_s is a function of Young's modulus (E), Poisson ratio (ν_t) and the value t_t/D, as defined in Eq. (1). In this work, the tube properties were chosen that were informed from

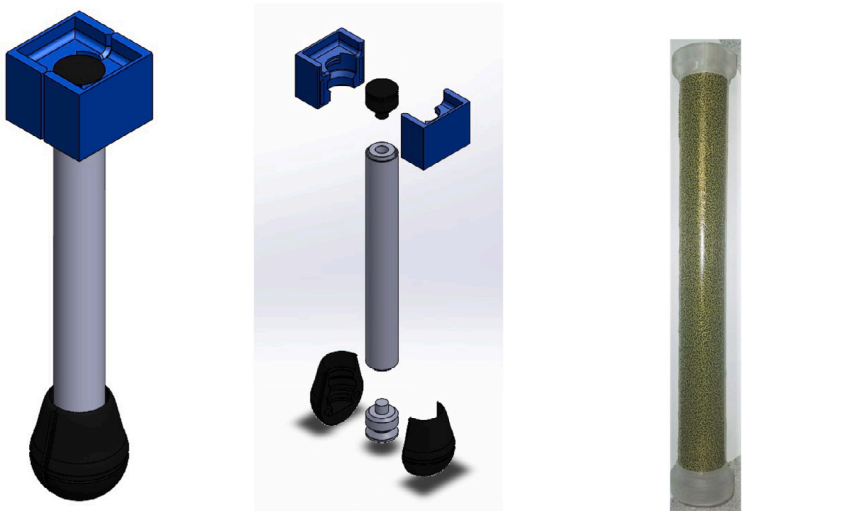

Fig. 2. Preparation of collapsible tube with a tattoo that facilitates stereo-photogrammetry.

Table 1
Tube properties reported in the literature and this study.

	Internal diameter D (mm)	Length L (mm)	Thickness t_t (mm)	L/D	t_t/D	Young's Modulus E (MPa)	Stiffness K_s (Pa)
Wu et al. (2015)	10	147	0.7	14.7	0.070	0.56	21
Wang et al. (2009)	12.7	120	0.33	9.45	0.026	1	2
Bertram and Tscherry (2006)	12	228	1	19	0.083	–	–
Truong and Bertram (2009)	13	213	1	16.4	0.077	–	–
Yiasemides et al. (2017)	8	52	0.25	6.5	0.031	1.25	4.2
Present study	25.4	254	2	10	0.079	1.55	85

previous studies listed in Table 1. In the current experiments, a larger tube geometry was used to facilitate better measurement of 3D tube geometry using stereophotogrammetry and the 2D velocity field using PIV. The tube had an internal diameter, length, and wall thickness of $D = 25.4$ mm, $L = 254$ mm, and $t_t = 2$ mm, respectively.

$$K_s = E\left(\frac{t_t}{D}\right)^3 \frac{1}{12(1-\nu_t{}^2)} \tag{1}$$

The preparation of the tube involved casting silicone into a mold of the desired shape and curing over a period of 24 h. The mold was first created using an internal circular rod and a concentric external pipe. The external pipe was manufactured in two halves, so cutting was not required to remove the cast tube. The internal rod and the external pipe were held in place and aligned using two symmetric stamps and an internal stamp with a pin that could be inserted into the internal rod. These components were used at both the top and bottom ends of the mold. The symmetric stamps at the bottom of the mold were designed to be round in shape to attach a collecting sack that prevented leakage of silicone. A layer of tape and dental glue was also applied to minimize leakage and increase cure time. Finally, after curing, the tube was removed from the mold and a speckle-patterned tattoo was installed on its external surface. The patterned tattoo was necessary to measure deformations in tube geometry using stereophotogrammetry. A schematic of the mold used to cast the silicone tube is shown in Fig. 2.

Next, the mechanical properties of the tube were quantified by measuring the Young's modulus of the silicone material used during the preparation of the tube. This was done by casting silicone into a rectangular mold and then the cured material was subjected to a static test. The stress–strain curve was obtained from the test, and Young's modulus was calculated within the linear region of the curve for a strain less than 10% of the original length. The Young's modulus was calculated to be 1.55 MPa. The silicone material used to prepare the tube involved Sylgard 184 and Ecoflex 00–30 mixed in a weight ratio of 5:1. This ratio was particularly chosen to obtain the desired Young's modulus. Based on the geometric properties of the tube, Young's modulus, and its Poisson's ratio ($\nu_t = 0.5$) the stiffness parameter K_s was calculated to be 85 Pa using the Eq. (1). During the installation of the tube within the pressure chamber, it was subject to axial extension of approximately 2 mm, which translate to an axial tensile force of 2 N during the experiments.

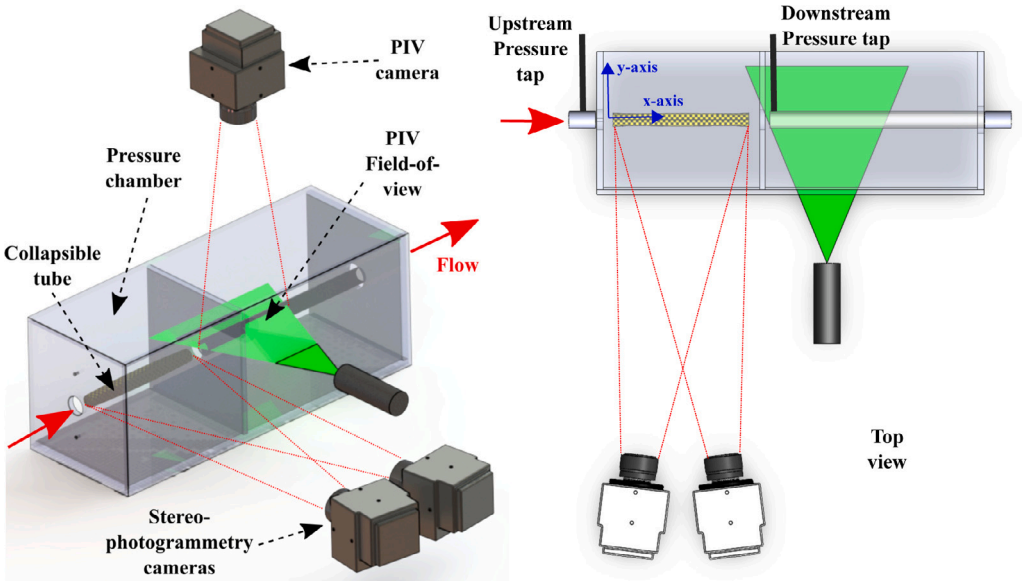

Fig. 3. Schematic of stereo-photogrammetry and PIV measurements.

2.3. Measurement techniques

2.3.1. Flow rate and static pressure

The flow rate (Q) through the tube was measured using an ultrasonic flow transducer (SonoTT™DIGIFLOW-EXT1). The tube was instrumented with the sensor 20 cm ahead of the upstream pipe. It was ensured that there was a straight section of pipe, 15 cm long, on either side of the flow meter, which guaranteed the accuracy of the measurements. The location of the flow meter in the flow loop is shown in Fig. 1. Pressure measurements were also made in the flow loop at two locations. The pressures p_{up} and p_{dn} were measured upstream (64 mm) and downstream (45 mm) of the collapsible tube, respectively, through pressure taps. These taps were attached to pressure transducers (Validyne DP15). The transducers were calibrated using a calibration/verification device (Delta-Cal 650–950). Both the flow meter and the two pressure transducers were connected to a data acquisition system (NI USB-6341) and simultaneously sampled for a duration of 5 s, at a rate of 1000 Hz. A pressure monitoring device (ReliOn 100–021 REL) was also suitably modified for the experiments to measure the external pressure of the tube p_{ex} in the pressure chamber. Uncertainties in the flow rate measurements are estimated to be within ±0.15 L/min, and pressure measurements to be ±0.1 kPa.

2.3.2. Stereo-photogrammetry

One of the key highlights of this study is the implementation of a stereophotogrammetry technique for the three-dimensional characterization of tube geometry. For this purpose, a speckle-patterned tattoo was first installed on the exterior surface of the collapsible tube. Next, two cameras (Phantom VEO 640) with a resolution of 2560 x 1600 pixels were aligned to be in the same horizontal plane as the tube axis and mounted with a lens, each having a focal length of 50 mm (see Fig. 3). The camera positions were adjusted so that each of their field of view covered the entire length of the tube, resulting in an optimal angular separation of approximately 10°. The cameras were controlled using Phantom Camera Control (PCC) software, and the acquisition of images was digitally synchronized using an external trigger signal. The trigger signal was generated from the timing unit used for the PIV measurements. The images were captured at a rate of 24 Hz and a duration of 6 s High-intensity LED lights were also used to illuminate the collapsible tube because the exposure time of the camera was short. For calibration, the tube was removed, and a checkerboard plate was inserted and traversed through the volume occupied by the tube in its fully-open state. The cameras captured images of the plate at different locations within this volume to obtain the calibration parameters. To ensure further accuracy, surface of a tube with a known geometry (in its fully open state) was reconstructed and compared against an ideal circular profile. These steps resulted in reconstructions with uncertainty bounds of ± 0.005D, for all the cross-sectional slices of the tube.

When the tube was carefully clamped onto the rigid pipes inside the pressure chamber it was ensured that its axis remained horizontal and was not subject to any residual torsional strain. Furthermore, the tube was mounted so that a circumferential location on both ends of the tube remained nearly at the same position on the mount. Every time the tube needed to be removed and installed back, the uncertainty in the twist between the ends of the tube was estimated to be within ±2° which translates to a residual torsional stress of ≤ 1.8% of hoop stress. This ensured the repeatability of the tube deformations about its axis. For the current experiments, the tube was aligned so that the largest surface area of the tube was visible to both cameras during collapse (refer to Fig. S1 in the Supplementary Material).

2.3.3. Planar Particle Image Velocimetry

The velocity field downstream of the collapsible tube was measured using the planar Particle Image Velocimetry (PIV) technique. A pulsed laser (Photonics DM30-527DH laser) served as a light source for this purpose. This dual-head laser generated a 527 nm beam that was converted into a sheet through suitable optics. A 1.5 mm thick laser sheet was used to illuminate a horizontal plane that passed through the axis of the downstream acrylic tube. The field of view started about 45 mm from the inlet of the collapsible tube and extended further downstream. To reduce the effects of optical distortions introduced by the curvature of the acrylic tube, the PIV chamber was filled with a 70–30 glycerin–water mixture, as mentioned earlier. The flow within the tube was seeded with fluorescent PMMA rhodamine particles with mean diameters of 63–75 μm. The light scattered from these particles was captured by a camera (Phantom VEO 4K 990L) in frame-straddled mode after it passed through an orange filter installed on a 50 mm lens. The camera was placed with its axis perpendicular to the laser sheet (see Fig. 3). The camera and laser were controlled using a Programmable Timing Unit (PTU) to adjust the time delay between laser pulses, and thereby obtain optimal particle displacements. The image pairs were captured and processed using LaVision DaVis software.

Additional challenges were experienced during PIV instrumentation in this study. First, optical distortions in the field of view of the camera were introduced due to the presence of a liquid–air free surface. This was overcome by introducing a supported horizontal acrylic window that replaced the liquid–air interface with a solid surface. Second, because of the unique field of view with a large aspect ratio, a high-precision calibration plate was custom-designed to fit into the downstream acrylic tube. It should be noted that synchronization across the different measurement techniques was achieved using a trigger signal supplied from the PTU of the PIV system.

2.4. Data processing

2.4.1. Stereo-photogrammetry

The stereo images were processed by means of MATLAB's Computer Vision Toolbox. The toolbox features automatic self-calibration based on the calibration images, which yielded both the intrinsic and the extrinsic camera parameters. With these parameters, the image pairs were rectified and then correlated to obtain a disparity map; in particular, the function 'disparitySGM' was used in this study. The disparity map was translated into a 3D point cloud of all pixels that were successfully correlated. The point cloud was then cleaned up by standard functions of the toolbox, which also included segmentation based on clusters of points, to remain with only the points that represented the surface of the collapsible tube. Uncertainties in the depth measurements obtained from stereophotogrammetry were estimated to be within ± 0.005D.

Along the top and bottom of the tube, the Digital Image Correlation (DIC) was unable to yield points such that only about 100° along the circumference of a circular tube was present in the point cloud. Based on a point cloud representing the non-collapsed state of the tube, the tube's axis was found by means of multi-variable optimization. The coordinate transformation that aligned the tube's axis with the x-axis and brought its center of mass into the x–y plane was used to align all other data sets in the same way. For slicing, volumes of finite thickness were defined at uniformly spaced locations along the tube axis. The points within each volume were projected onto the volume's mid-plane. A single longitudinal slice in the x–y plane was obtained by the same method.

The cross section of each slice was reconstructed by reflecting its points about the origin and fitting a π-periodic smoothing spline through them, in polar coordinates. For highly collapsed cross-sections which in polar coordinates had an undercutting shape, a transformation of the azimuthal coordinate was done before spline fitting. The spline was evaluated at a number of locations in transformed space and the resulting coordinates were transformed back into physical space.

The internal shape of the cross-section was reconstructed as an offset from the external shape by the known wall thickness, neglecting any possible variations in local wall thickness. This assumption was justified by the large ratio of the circumference to the wall thickness of the collapsible tube. The cross-sectional area of the internal shape was computed with MATLAB's polyarea function. In some cases of severe collapse, the reconstructed internal shape intersected itself. This indicated that the collapse was, in fact, not perfectly symmetric. The region of self-intersection was excluded from the area computation because it would yield a negative contribution. The steps involved are summarized in the schematic in Fig. 4.

2.4.2. Planar particle image velocimetry

The image pairs captured for PIV at 24 Hz with a duration of 6 s were processed in multiple passes using LaVision's DaVis software. An interrogation window of 64 × 64 pixels with an overlap of 50% was used in the first pass. A window of size 32 × 32 pixels with a 75% overlap was used in the final four passes, which yielded a vector resolution of 0.44 × 0.44 mm (0.017D × 0.017D). Further processing was performed to remove spurious vectors. The uncertainties in the velocity measurements were calculated to be less than 4% of the maximum magnitude of the velocity in all cases (< 0.016 m/s).

2.5. Experiment campaigns

Experiments were conducted in two separate campaigns. All the measurements made during this study were within the laminar flow regime. The purpose of the first campaign was to characterize the response of the tube to different flow conditions and to identify the distinct operating regimes, i.e. open, collapse, and oscillating. The second campaign involved the detailed measurement of the tube geometry and flow field properties simultaneously to address the correlation between the two. At the end of each experiment, the kinematic viscosity of the fluid (ν_f) was also measured and found to be 17 cSt. Detailed information on flow/operating conditions is summarized in Table 2. Here Reynolds number (Re_D) and non-dimensional stiffness (β) are defined

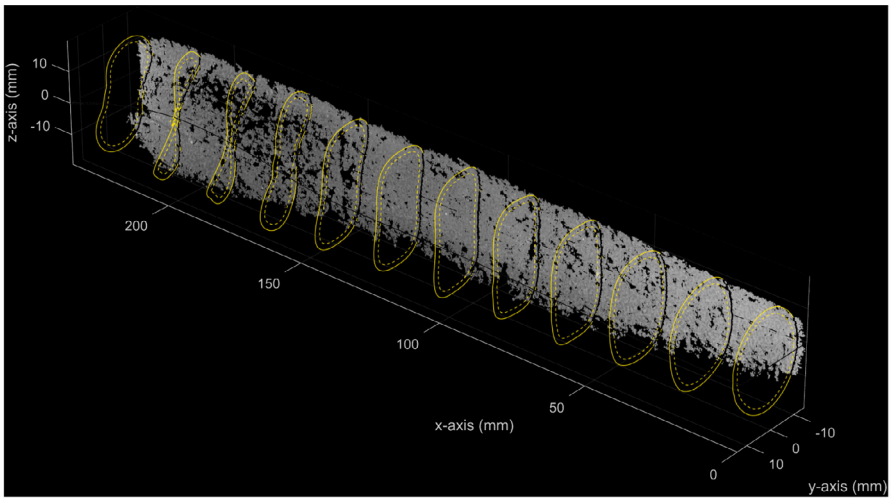

(a) Point cloud reconstruction of tube surface obtained from stereo photogrammetry along with slices of cross-sections extracted

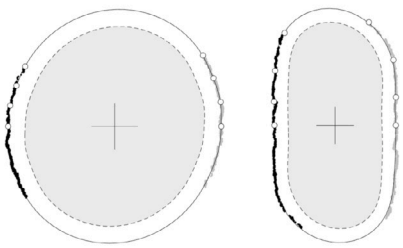

(b) Extraction of tube inner cross-section from point cloud reconstruction using guide-points and spline interpolation. Surface features considered to be symmetric about axis.

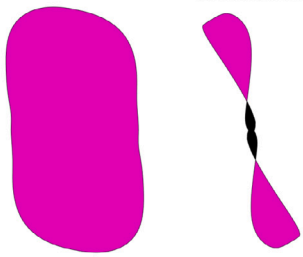

(c) Calculation of tube inner cross-sectional area at different conditions of collapse. In the event of overlap, black central region is disregarded during the calculations

Fig. 4. Preprocessing and geometric data extraction from point cloud reconstruction of stereo photogrammetry data.

Table 2
Summary of experimental conditions for data acquisition. Density of fluid $\rho_f = 1180$ kg/m^3.

	Flow rate, Q (L/min)	Transmural pressure, Δp_{tr} (kPa)	Reynolds number, Re_D	Non-dimensional stiffness, β	Stereo photogrammetry	Planar PIV
1	7.2	5.34	353	1.28	–	–
2	7.4	7.04	363	1.22	–	–
3	7.9	6.27	390	1.05	✓	✓
4	7.9	4.70	390	1.05	–	–
5	8.1	3.85	400	1.00	–	–
6	8.8	6.26	433	0.86	–	–
7	9.2	6.09	449	0.79	–	–
8	9.4	5.89	460	0.76	–	–
10	9.6	6.42	469	0.73	–	–
11	9.9	5.54	487	0.67	–	–
12	10.3	5.20	503	0.63	✓	✓
13	11.9	3.87	584	0.47	✓	✓
14	12.3	4.51	604	0.44	–	–
15	12.3	5.21	604	0.44	–	–
16	12.6	3.26	617	0.42	–	–
17	14.1	4.49	692	0.33	–	–
18	14.4	4.13	707	0.32	–	–

in Eq. (2), where ρ_f is the density of the working fluid, U_{avg} is the bulk velocity at the inlet, K_s is the stiffness of the collapsible tube defined in Eq. (1), L and D are the length and diameter of the collapsible tube, respectively.

$$Re_D = \frac{U_{avg} D}{\nu_f} \qquad \beta = \frac{K_s}{\rho_f U_{avg}^2} \tag{2}$$

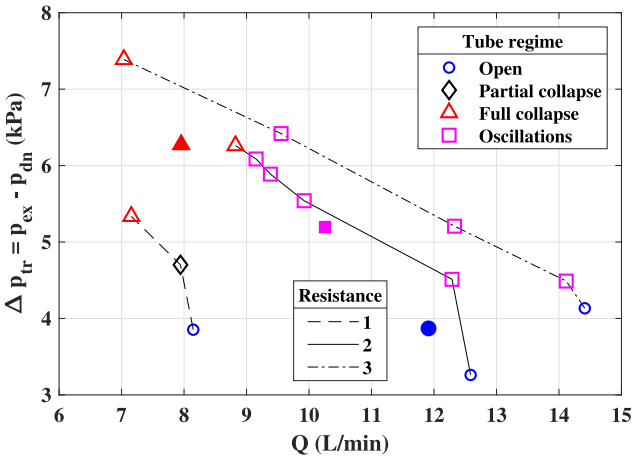

Fig. 5. Transmural pressure versus flow rate diagram identifying the different regimes. Filled markers represent conditions at which simultaneous measurements of tube geometry and flow field were performed.

3. Results

3.1. Regime identification

To characterize the response of the tube to different flow conditions, the variations in flow rate with transmural pressure were quantified under different conditions of upstream resistance (percentage of valve opening), while also taking visual note of the state of tube collapse. Basically, in the first step, the upstream resistance (R_1) was set to a certain flow rate. Then the external pressure p_{ex} was gradually increased to fixed values and the state of the tube was regularly observed to identify any visual changes in its geometry, from an open state to a fully collapsed state. At each of these conditions, the flow rate (Q), upstream pressure p_{up}, downstream pressure p_{dn} and external pressure p_{ex} are probed and recorded. This process was repeated for two more conditions of upstream resistances R_2 and R_3, such that $R_3 < R_2 < R_1$. In this manner, the tube states corresponding to fully open (blue circular markers), fully collapsed (red triangular markers), partially collapsed (black diamond marker) and oscillations (magenta square markers) are plotted at their corresponding values of flow rate and transmural pressure, as shown in Fig. 5.

The results indicate that in each case of fixed upstream resistance, an increase in transmural pressure p_{tr} leads to a corresponding increase in resistance to flow and therefore a decrease in flow rate. At high upstream resistance (R_1), the tube transitions from a fully open state to a fully collapsed state without any intermediate states with oscillations. This is justified by the fact that, under these conditions, low flow rates translate to low fluid momentum. Therefore, a partial tube collapse is observed in this state. Furthermore, at this high upstream resistance (R_1), the flow rate drops by only a small value due to the increase in external pressure.

On the other hand, at lower upstream resistances R_2 or R_3, the tube transitions from fully open to fully collapsed state through the intermediate condition of oscillations, when the transmural pressure p_{tr} gradually increased. The higher flow rate and fluid inertia at these upstream resistances contribute to the interaction with the tube structure. Finally, by generating the flow rate — transmural pressure diagram, tube oscillations are found to occur beyond a critical Reynolds number of 430.

Based on these results, flow conditions that correspond to three distinct regimes are identified, namely, fully open, fully collapsed, and oscillating. At these operating conditions (represented by the filled markers in Fig. 5), the next experimental campaign was carried out where the geometry of the tube and the downstream flow field were measured simultaneously. Each of these regimes is discussed individually in the upcoming sections. Before characterizing the individual regimes, tube cross-section area was measured and mapped as a function of the transmural pressure to compare against the classic Tube law (refer to Fig. S2 in supplementary material).

3.2. Open-tube regime

To characterize this regime, the geometric features are first extracted from the stereo-photogrammetric reconstruction of the tube, as described in Section 2.4.1. This is followed by a discussion of the flow field properties. Since, under this regime, there are no temporal dynamics involved, time-averaged properties are analyzed. In Fig. 6(a) the variation in the time average values of the inner cross-sectional area and the perimeter is plotted along the length of the tube. Both these parameters are normalized with respect to their ideal values corresponding to a circular cross-section of 25.4 mm diameter. The results indicate that both the cross-sectional area and the perimeter do not change along the length of the tube and remain close to a value of 1, as expected. To determine the inner shape of the tube, the cross-sectional profiles are plotted at multiple streamwise locations (upstream, midway, and downstream) along the tube as shown in Fig. 6(b). Clearly, the cross-sectional profiles of the tube closely match the ideal circular

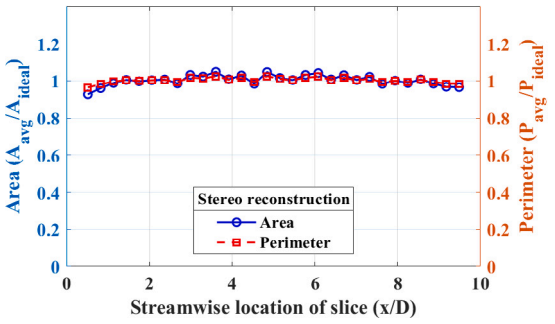

(a) Variation in mean inner cross-sectional area and perimeter along the length of the tube

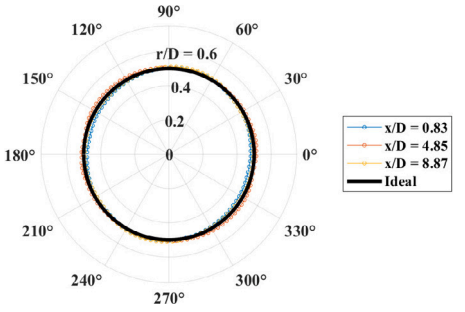

(b) Mean inner tube cross-sectional profiles at different locations along length of the tube

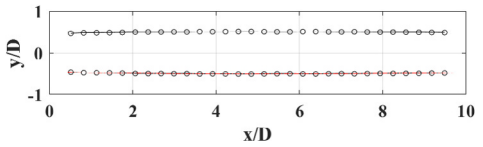

(c) Averaged longitudinal slice of inner cross-section of the tube at mid plane (z = 0)

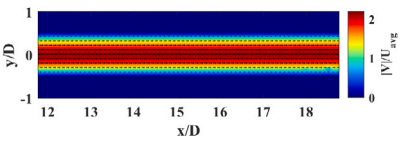

(d) Mean velocity field in the downstream section of the tube

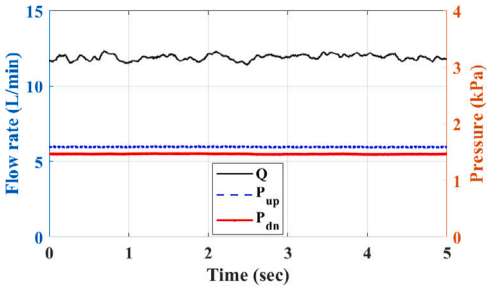

(e) Temporal evolution of flow rate, upstream pressure and downstream pressure

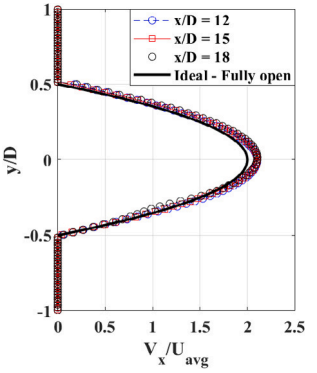

(f) Streamwise velocity distribution (averaged) in the cross-stream direction

Fig. 6. Geometric and fluid flow properties when the tube is in fully open regime for Reynolds number $Re_D = 584$. Note: Velocities are normalized with respect to the average flow velocity in the tube under fully open regime.

shape with a diameter of 25.4 mm. Similarly, a streamwise slice of the tube along the midplane (z/D = 0) in Fig. 6(c) shows minimal variation in radii along the tube length. This confirms that all cross-sectional profiles in the streamwise direction are also identical.

Next, the flow field downstream of the tube is examined by mapping the time-averaged velocity field in Fig. 6(d). The left edge of the PIV field of view is about $1.75D$ downstream from the end of the collapsible tube. The velocity contours plotted are normalized with respect to the average velocity calculated based on the average flow rate measurement. The velocity contours indicate the presence of a peak velocity close to the axis of the tube, which rolls off towards the tube walls. In addition, a uniform distribution along the streamwise direction is observed. Since this velocity profile is representative of a Poiseuille flow, it is verified by extracting the cross-stream distribution of the streamwise velocity V_x, at several streamwise locations along the tube. These velocity profiles are then compared with the ideal Poiseuille flow profile, as shown in Fig. 6(f). Apart from a nominal difference in peak velocity with respect to the ideal value, at the tube axis, the velocity distributions are indicative of a fully developed laminar flow. This difference is likely due to the uncertainty in the flow rate measurements.

In addition to velocity field measurements, the flow rate and upstream and downstream pressures were also recorded simultaneously. Fig. 6(e) shows that none of these flow properties experiences any changes with time. Although the average flow rate is measured to be 11.91 L/min, the mean pressure drop between pressure taps upstream and downstream ($P_{up} - P_{dn}$) is found to be 0.125 kPa. Based on this flow rate value, the average flow velocity is calculated to be 0.392 m/s. At the same time, the length of the tube (L) over which this pressure drop occurs is calculated from the first principles using the Eq. (3).

$$P_{up} - P_{dn} = \frac{8\pi\mu_f LQ}{A^2} \tag{3}$$

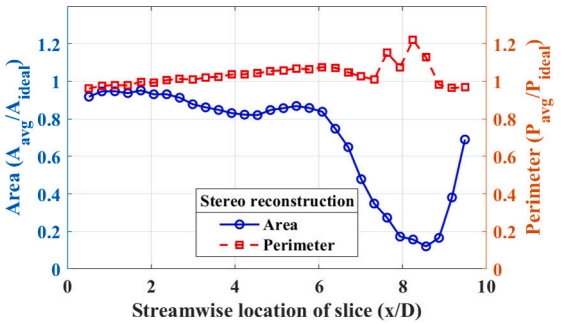

(a) Variation in mean inner cross-sectional area and perimeter along the length of the tube

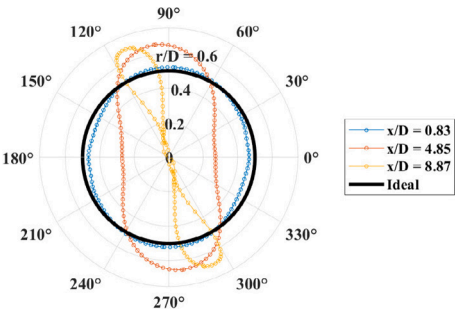

(b) Mean inner tube cross-sectional profiles at different locations along length of the tube

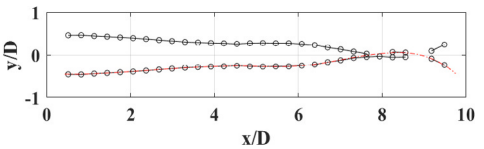

(c) Averaged longitudinal slice of inner cross-section of the tube at mid plane (z = 0)

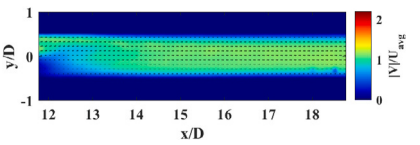

(d) Mean velocity field in the downstream section of the tube

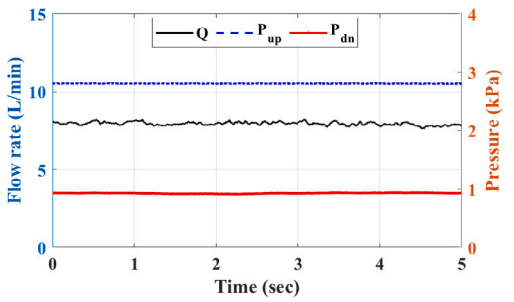

(e) Temporal evolution of flow rate, upstream pressure and downstream pressure

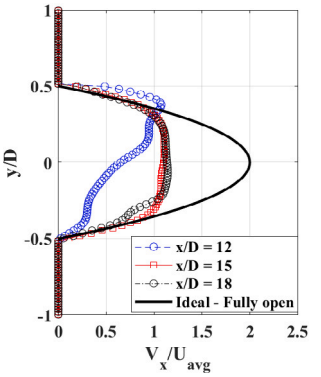

(f) Streamwise velocity distribution (averaged) in the cross-stream direction

Fig. 7. Geometric and fluid flow properties when the tube is in fully collapsed for Reynolds number $Re_D = 390$. Note: Velocities are normalized with respect to the average flow velocity in the tube under fully open regime.

Here, μ_f is the dynamic viscosity of the fluid and A is the cross-sectional area of the tube. The value of L calculated to be 0.32 m is found to be very close to the physical distance between the pressure taps (0.36 m). Therefore, the flow through the collapsible tube in the fully open regime behaves essentially similarly to the flow through a solid circular pipe.

3.3. Closed-tube regime

From Fig. 5 it is identified that when the transmural pressure p_{tr} is sufficiently large, the tube is visually observed to experience complete collapse. To quantify this, the time-averaged internal cross-sectional area and perimeter of the tube are calculated at several locations along the length of the tube and plotted as shown in Fig. 7(a). As mentioned above, the two parameters are normalized by their respective values for an ideal (circular) cross section of 25.4 mm diameter. At the upstream locations (x/D → 0), both the normalized tube perimeter and the cross-sectional area have values close to 1. This is indicative of the nominal deviation of the tube from the circular profile due to its proximity to the clamped end. As one moves further along the x-axis, due to a high value of transmural pressure, the perimeter of the tube still hovers around 1 while the cross-sectional area gradually decreases to 0.8, until about x/D = 6. Beyond this streamwise location, the cross-sectional area of the tube decreases dramatically and achieves maximum collapse close to x/D = 8.5. In this region, the perimeter is seen to experience a few streamwise fluctuations. However, this is expected to be due to artifacts of interpolation performed while reconstructing the opposite (non-visible) face of the tube and its upper and lower regions. This could not be completely avoided because of the geometric constraints of viewing and reconstructing

a portion of the tube that is nearly flat in this region of interest. Beyond this region, the cross-sectional area of the tube starts to increase back towards the ideal value.

The cross-sectional profiles of the tubes plotted in Fig. 7(b) also corroborate the observations regarding the cross-sectional areas. At the upstream location (x/D = 0.83), the tube section is nominally circular in shape. As one moves along the streamwise direction, the tube profile is closer to an ellipse at x/D = 4.85, and a dumbbell profile with complete collapse at the center, at x/D = 8.87. A longitudinal slice along the mid-plane of the tube (z/D = 0), as seen in Fig. 7(c), also indicates that the tube experiences a gradual reduction in the lateral dimension until x/D = 6. Beyond this, there is complete constriction around x/D = 8, and gradual enlargement after that.

Downstream of the collapsible tube, the time-averaged velocity field is computed and normalized with respect to the average velocity under the fully open regime, as shown in Fig. 7(d). Here, there is a reduction in the magnitude of velocity throughout the field of view, when compared to a fully-open tube regime. Further, just downstream of the collapsible tube, the flow also appears to be preferentially oriented towards one side (upper wall) of the tube, with a low velocity region on the other wall. This is potentially because the downstream tube cross-sections exhibit axes of collapse that are marginally titled with respect to the PIV measurement plane. This is evident in the cross-stream velocity profiles seen in Fig. 7(f). However, this asymmetry in velocity distribution about the tube axis completely subsides by 5 diameters from the end of the collapsible tube. Finally, the peak velocity in the field of view is nearly half that observed in the fully-open regime. This is also confirmed by the reduction in flow rate from 11.91 L/min to 7.95 L/min, as seen in Fig. 7(e). The throttling of the flow is also accompanied by a significant increase in pressure drop across the ends of the collapsible tube $P_{up} - P_{dn} = 1.864$ kPa.

3.4. Oscillatory-tube regime

Although the fully open and closed regimes exhibit the limiting cases, an intermediate transmural pressure can lead to self-excited oscillations in the tube. These can manifest themselves in the form of fluctuations in the geometric properties of the tube and the flow field. Since pressure and flow rate are lower-order measurements that are acquired at a much higher frame rate, these are first closely examined in Fig. 8(a). On the one hand, the temporal evolution of the flow rate Q and the upstream pressure p_{up} indicates that these parameters remain nearly constant throughout. This suggests that any flow field fluctuations within the tube are either not propagated upstream or die down by the time they reach the location of these transducers. Similar observations are reported by Bertram et al. (2008) regarding the flow rate, who suggest that the reduced pulsatility in the upstream regions may be associated with the compliance of the tube upstream of the throat, where the displaced fluid could be temporarily stored. It is likely that this argument holds, since we shall see in later discussion that the tube geometry also experiences fluctuations that gradually decrease in amplitude as one moves upstream along the tube. On the other hand, downstream pressure p_{dn} exhibits periodic fluctuations of type LU, described by Bertram et al. (1990). These fluctuations have a low frequency of the order of 1 Hz, and the area trace appears to spend a longer duration above the mean pressure compared to the trace below the mean pressure, as seen in in Fig. 8(a).

Since downstream pressure fluctuations are periodic in nature, distinct points corresponding to four phases are identified in each cycle to be able to correlate with variations in tube geometry and flow field properties. The first and third phases correspond to the local minima and maxima in each cycle, respectively. Next, the time instants at which the curve passes the mean pressure during rise time and fall time are represented as the second and fourth phases, respectively. In this manner, each of the four phases is overlaid on the pressure plot, by different markers in Fig. 8(a).

First, the temporal evolution of a tube cross section close to the downstream end of the tube (x/D = 9.17) is traced in the different phases in Fig. 8(b). In the first phase (t/T = 0.01), the cross-section of the tube resembles a shape that transitions from a dumbbell to an elliptical profile. Here, T represents the average cycle time period measured to be 1.143 s. In the next phase (t/T = 0.23), the tube expands along the minor axis (of the ellipse), while its size nominally decreases about the major axis (perpendicular to the minor axis). The tube in this phase is elliptical in shape. In the third phase, the tube still resembles an elliptical shape, whereas its dimension along the minor axis decreases marginally, and that along the major axis increases by a small amount. In the final phase, the tube transitions back to a dumbbell profile, this time with the smallest dimension on the minor axis and the largest on the major axis. Refer to Fig. S3 and S4 in the Supplementary Material and the attached clip 'PointCloundVideo.avi' for evolution in tube cross-sections at other locations along the tube. These transitions in the tube geometry very closely resemble the small-amplitude oscillations of Type-II about one of the non-axisymmetric equilibrium states, as reported by Heil and Waters (2006). Note that these oscillations are also reported as a Type-A by Heil and Boyle (2010).

Similarly to tube cross-sectional profiles, the streamwise distribution of cross-sectional areas is plotted at different phases of the cycle in Fig. 8(c). In the first phase, the area normalized with respect to the area of an ideal circular shape of the tube, reaches a minimum value of approximately 0.2, at a streamwise location of x/D = 8. In the second phase, the throttling area changes to an upstream location (x/D < 8) while also having an increase in magnitude (0.4) compared to the previous phase. During the next two successive phases, the tube cross-section progressively decreases and its location reaches the farthest position downstream (x/D ≈ 8.5). Essentially, the throttling cross-section of the tube periodically changes position such that the largest collapse occurs at the farthest downstream location within the tube, over the full cycle.

Next, the contour maps of the normalized streamwise velocity (V_x/U_{avg}), just downstream of the collapsible tube are plotted at different phases of one full cycle in the oscillation of the tube, in Fig. 9. At phase t/T = 0.02, which is briefly after the local minima in the downstream pressure, the streamwise velocity field downstream of the collapsible tube exhibits a low-velocity region at the entrance of the tube. This is followed by a gradual increase in velocity within the field of view over successive phases. However, by t/T = 0.35, a distinct wave of streamwise advecting fluid is evident. This wavefront is observed to convect downstream over

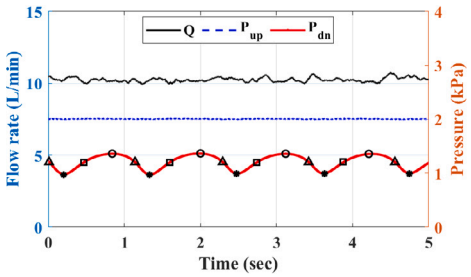

(a) Temporal evolution of flow rate, upstream pressure and downstream pressure. Markers indicate four phase during each cycle.

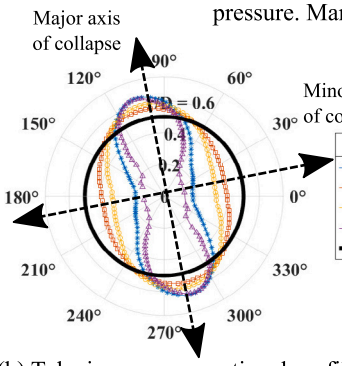

(b) Tube inner cross-sectional profiles at different phases indicated in (a)

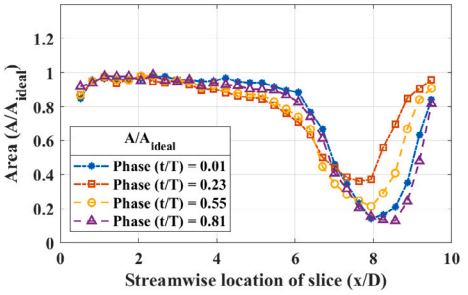

(c) Streamwise variation in tube inner cross-sectional area at different phases indicated in (a)

Fig. 8. Phase portraits of geometric and fluid flow properties when the tube is under self-excited oscillations for Reynolds number Re_D = 503. The symbols 'asterisk','square','circle' and 'triangle' represent the phases, t/T = 0.01, 0.23, 0.55 and 0.81, respectively. Cycle time period, T = 1.143 s.

several phases and nearly fill the entire field of view by the time around t/T = 0.57. This phase also corresponds to the instant right after the downstream pressure peak is reached. Beyond this phase, high-velocity regions persist over successive frames and then start decaying, from the entrance region. Closer to the phase t/T = 0.9, we also observed the two-jet flow closer to the walls, with a low-velocity region close to the tube axis. These jets appear to merge further downstream into a single stream. Qualitatively these features closely resemble the observations made by Bertram et al. (2008), in the flow field downstream of an oscillating collapsible tube at low Reynolds number. Interestingly, the retrograde flow reported by Bertram et al. (2008) and Yiasemides et al. (2017) is not as prevalent in the current study. These regions were generally small and spatially local to the walls of the tube. The observed dissimilarities may be attributed to differences in tube geometry in the respective studies (see Table 1). Furthermore, the retrograde flow persists only periodically in this study and only for a very short duration over a period of oscillation of the tube. Velocity measurements made by Yiasemides et al. (2017) inside the tube immediately downstream of the throat, in a plane perpendicular to the one measured in this study, indicate that just when the downstream pressure starts to fall from its peak value, the centerline velocity experiences a sharp decline close to the throat. The velocity then gradually increases close to downstream end of the tube where the tube cross-sectional profile recovers. A similar observation can be made from the velocity contours in Fig. 9 after the peak pressure is achieved and starts declining (t/T > 0.55). However, the reduction in velocity does not occur immediately because of the time taken by the flow to advect through the downstream section of the tube.

If one closely examines the trends in the variations in the velocity field, the downstream pressure fluctuations, and ultimately the oscillations in the tube geometry, there appears to be phase-relationship between these parameters. A consistent phase lag can be expected to exist between fluctuations in tube geometry and flow field properties, which is explored by studying the spectral properties and correlations between the two.

First, the downstream pressure P_{dn} is used as a first-order metric to characterize flow field fluctuations since it is sampled at a significantly higher frame rate (1000 Hz) than the velocity field (24 Hz). The power spectra for the downstream pressure are computed and plotted as shown in Fig. 10(a). This plot indicates the presence of a single dominant mode at a frequency of about 0.8 Hz. This dominant mode is also exhibited globally in fluctuations in tube geometry, as seen in the power spectra of the fluctuations in the cross-sectional area, in Fig. 10(a).

Next, in order to discern the mechanisms associated with fluid–structure interactions in this oscillating tube regime, correlations and phase relationships between geometric and flow field parameters are quantified. These geometric parameters include fluctuations in the inner cross-section of the tube along its minor and major axes (Fig. 8(b)). The flow parameters studied include the downstream pressure and the velocity field.

In the first stage, each point on the inner surface of the minor axis of collapse of the tube is extracted along its length (x-axis), and its temporal evolution is obtained (refer Fig. S5 in the Supplementary Material). Then, the mean values of inner-radii along the

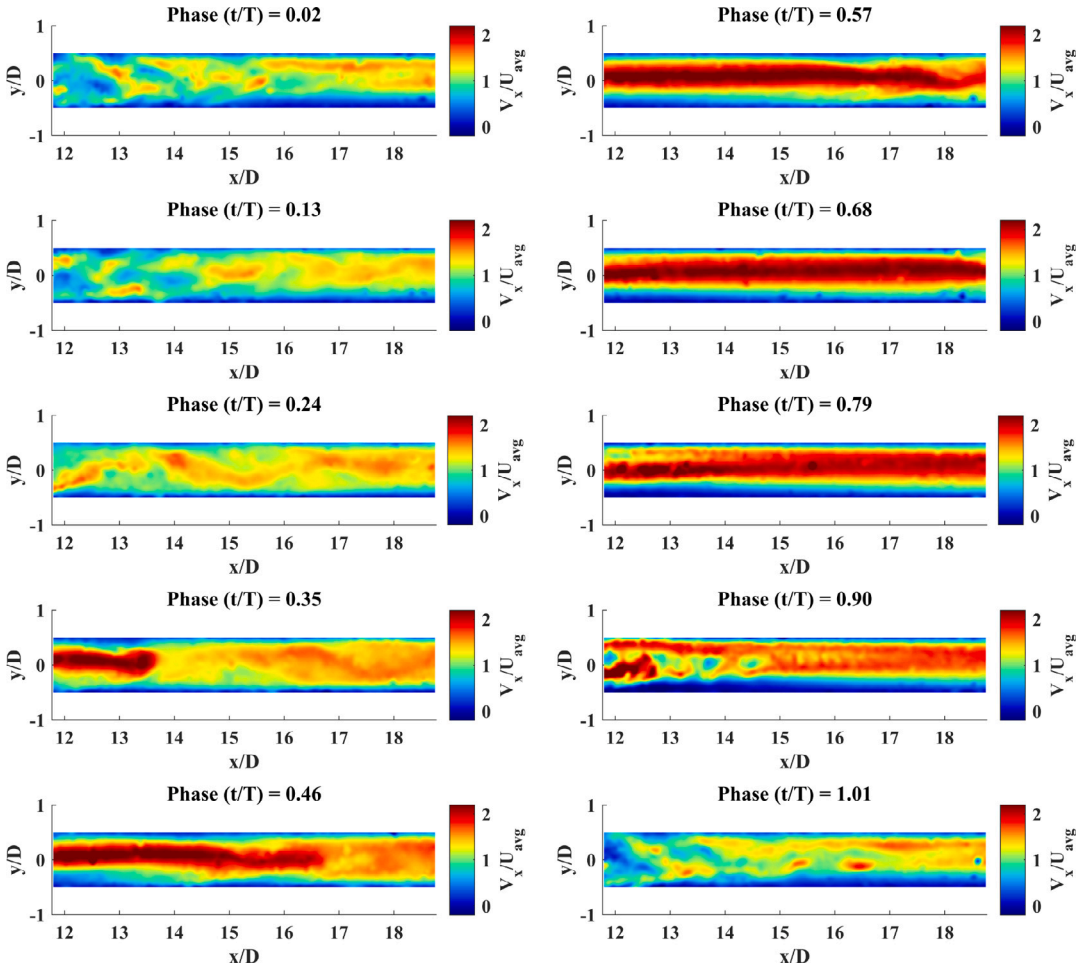

Fig. 9. Phase portrait of steamwise velocity contours for Reynolds number $Re_D = 503$. Note: Velocities are normalized with respect to the average flow velocity in the tube under a fully open regime. Flow is from left to right. Cycle time period, $T = 1.143$ s.

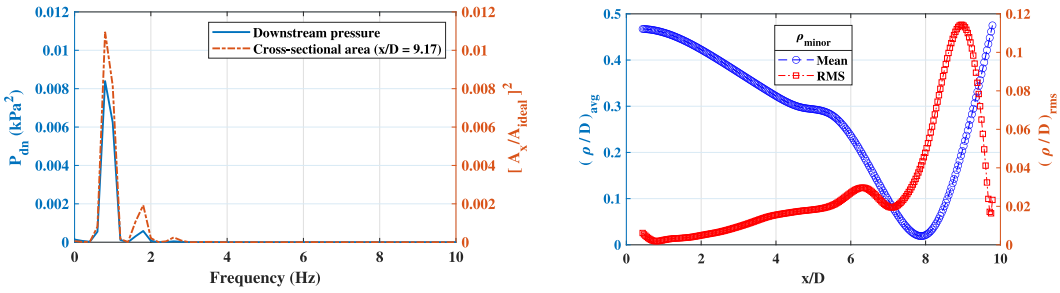

(a) Power spectra (b) Minor axis mean and RMS

Fig. 10. Metrics of fluctuations in tube geometry and flow field.

minor axis of tube collapse are computed at each streamwise location and plotted as shown in Fig. 10(b). Similarly, the root mean square (RMS) of the fluctuations in the radial coordinate of this surface is quantified and plotted against tube length in Fig. 10(b). This plot indicates that the inner radius of the tube along the minor axis of collapse starts at 0.5D at the upstream end where it is mounted onto a rigid pipe and gradually reduces to about 0.01D around x/D = 8. This region represents the mean position of the tube throat. Beyond this point, it increases sharply to 0.5D at the downstream end, where the tube is attached to a rigid pipe. On the other hand, fluctuations in the inner radius along the minor axis of collapse exhibit the opposite trend. Variations in tube radii

Table 3
Correlation coefficients (ρ), phase relationship (t/T) and p-value between tube geometric properties (x/D = 9.17) and flow properties.

Parameter	Major axis (r_{major})	Downstream pressure (P_{dn})
Minor axis (r_{minor})	$\rho = -0.95$ $t/T = 0$ p-value < 0.01	$\rho = 0.381$ $t/T = 0.146$ p-value < 0.01
Major axis (r_{major})	–	$\rho = -0.355$ $t/T = 0.146$ p-value < 0.01

are very small near the upstream and downstream ends, whereas large amplitude fluctuations are seen close to x/D = 9. Clearly, the streamwise location of the largest mean collapse in the tube and the largest oscillations are distinct. This is indicative that the effect of tube geometry on the downstream flow field may be dissociated into their respective mean and unsteady components. Therefore, the mean velocity field downstream of the collapsible can be related to the mean geometry of the throat, and the flow field fluctuations can be dictated by the largest oscillations in the throat. However, the oscillations in the geometry of the tube do not occur just along one of its axes.

Subsequently, the signals corresponding to the fluctuations in the tube radii along its minor axis of collapse are mean-subtracted and each of these is correlated with the fluctuations along the tube's major axis of collapse, at a cross-section close to the outlet of the tube (x/D = 9.17). The time series signals of the oscillations in the tube radii about the two axes are cross-correlated with each other and the downstream pressure fluctuations, to quantify the correlation coefficient and phase lag between the signals of interest. These are summarized in Table 3.

First, the correlation coefficient is quantified between tube deformations on the minor and major axes. This is found to have a value of −0.95, with a p-value less than 0.01. The negative value of the correlation coefficient indicates that any enlargement along the minor axis results in a corresponding contraction along the major axis, and vice versa. The phase lag between the two deformations is measured to be 0, as anticipated, since both these fluctuations occur on a single cross-section of the tube. These are indicative of the Type-A oscillations as reported by Heil and Boyle (2010).

Similarly, the phase delay between fluctuations along the minor axis and the downstream pressure is measured to be approximately t/T = 0.146. Therefore, disturbances introduced into the flow due to oscillations in the tube, take a time of about 0.17 s to cover the physical distance of 2.58 D, between the tube cross-section and the pressure tap. This yields a disturbance propagation speed of 0.39 m/s. It should be noted that the average fluid velocity calculated from the flow rate measurements made upstream of the collapsible tube yields 0.34 m/s. Based on the measured cross-sectional area at the streamwise location x/D = 9.17, the average velocity at this cross-section can be calculated to 0.40 m/s using the continuity equation. The fact that the flow velocity and the propagation speed calculated through the correlation between the tube geometry and downstream pressure are very similar suggests that the disturbances propagate essentially as a result of the advection of fluid through the tube.

Finally, the correlation coefficients between the tube radii along the minor and major axes of collapse with the downstream pressure are computed to be 0.381 and −0.355, respectively, with p-values less than 0.01. Although these correlation coefficients do not reveal a strong linear relationship between signals, a positive correlation coefficient between the minor axis and the pressure signal suggests that an enlargement of the throat dimensions along the minor axis of the tube leads to a corresponding increase in the downstream pressure. Similarly, constriction about the minor axis throttles the flow and thereby reduces the fluid pressure downstream. Furthermore, the oscillations in tube radii along the minor axis also exhibit a larger amplitude compared to the fluctuations along the major axis, as seen in the phase portraits in Fig. 8(b). Therefore, the collapse along the minor axis of the tube dictates the throttling of the flow and is expected to influence the global flow field fluctuations.

While it is established that one of the primary sources of flow field fluctuations downstream of the collapsible tube is due to oscillations in its minor axis of collapse, it should be remembered that the fluctuations are not local to a specific location along the length of the tube. It is imperative that the phase relationship between the oscillations at different locations along the tube be assessed. To do this, the time-series signals of the displacements along the minor axis of collapse of the tube are extracted at several positions along the tube. The signals are then cross-correlated with the fluctuations measured at x/D = 9.17. The correlation coefficients, p-values, and the phase difference between the different locations with those at x/D = 9.17 are plotted along the tube, as shown in Fig. 11. At the downstream end of the tube between x/D = 8 and 9.5, large positive correlation coefficients ≈ 1 are observed. This suggests that the tube deformations in this region are strongly coupled. As we move upstream, the correlation coefficient drops dramatically and becomes negative around x/D = 7. This represents a region that lies upstream of the locations of the largest collapse in the tube (x/D ≈ 8). The lowest correlation value of about −0.7 is achieved at x/D = 6, beyond which it starts to increase again to 0. The inversion in the sign of the correlation coefficient at x/D = 7 suggests a change in the direction of oscillations on the surface of the tube along its length. It should be noted that the correlations performed between different axial locations with those at x/D = 9.17 have p-values lower than 0.01 at most of the streamwise locations except in the region of x/D $\approx$ 2.5. This confirms that the calculated correlation coefficients are statistically significant in these regions.

Next, the phase relationship between the fluctuations at each streamwise location on the minor axis of the tube with that at x/D = 9.17 is evaluated. At further downstream locations (x/D = 8 to 9.5), a phase delay of zero is measured. This shows that

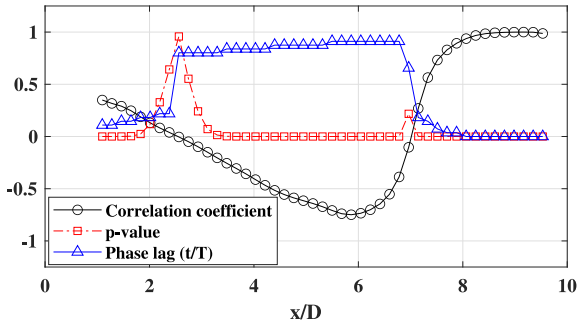

Fig. 11. Correlation coefficient and phase relationship quantified between tube surface fluctuations measured along the minor axis of the tube at the streamwise location of x/D=9.17, with the fluctuations measured along the minor axis of the tube at other streamwise locations in the tube. Flow condition is at a Reynolds number $Re_D = 503$. The p-values indicate the statistical significance of the correlation coefficients calculated.

the strongly coupled oscillations of the tube in this region occur synchronously in-phase. At a slightly upstream location where the correlation coefficient changes from 0 to negative values, the phase lag jumps up to t/T ≈ 1. This sharp increase is representative of the phase folding from 0° to 360°, suggesting that the oscillations upstream and downstream of x/D = 7 all occur in the same phase. In the range spanning x/D = 2.5 to 6.5, the phase delay remains nearly constant and shows the absence of a characteristic phase/disturbance propagation speed on the tube. Around x/D = 2.5, the phase delay decreases to a value close to zero. This is verified by the absence of any oscillations as seen in Fig. 10(b).

A careful observation of Fig. 10(b) and Fig. 11 brings to our notice, three important streamwise length scales in the tube: (1) x/D = 7, is the position in the tube that exhibits a shift in the direction of oscillations on its either sides; (2) x/D = 8, corresponds to the location in the tube with the largest mean collapse; and (3) x/D = 9, is the location with the largest amplitude of oscillations. Although these are certainly useful metrics for understanding the implications on the flow field, one must also take into account the fact that the position of the throat itself is dynamic. To investigate this, we take advantage of the unique 3D data acquired in this study to develop a time trace of the position of the throat over one cycle of oscillation of the tube, as shown in Fig. 12. The positions of the throat are extracted by identifying the location of the local minima in the radius in a streamwise cross-sectional slice of the tube at z = 0. Then the x/D and y/D coordinates of the throat are traced over a sequence of time frames within one full period of oscillation of the tube. Furthermore, the time instances corresponding to the different phases of downstream pressure fluctuations seen in Fig. 8(a) are also plotted. The ‘asterisk’ and ‘circle’ symbols represent the instants at which the minima and maxima are found in the downstream pressure fluctuations, respectively.

The time trace of throat seen in Fig. 12 exhibits oscillations along both the steamwise (x/D ≈ 0.6) and cross-stream directions (y/D ≈ 0.1). As one begins the trace starting with the position of the largest collapse (right-most corner in plot), with progression in time, the throat starts rapidly moving upstream (leftwards). At the same time, the cross-stream position of the throat moves farther from the axis of symmetry (x/D = 0) and achieves the highest value in the farthest upstream position. The streamwise displacement of the throat is about 7.5% of the supported tube length. In the next half of the cycle, the throat starts returning back towards the downstream extremum, as it converges towards the smallest cross-stream position where it originally started. The displacement of the throat during the returning part of the cycle occurs over a path that is not identical to the onward route. Instead, it cuts across the onward path by taking a slower and longer route. This correlates with the observed LU-type downstream pressure fluctuations, where the trace of the signal expends a longer duration above the mean pressure. The relevance of the variations in the geometric and flow field properties measured is discussed in the next Section 4.1.

4. Discussion

4.1. Flow-geometry relationship in oscillating regime

The trends observed in the correlation coefficients (Fig. 11) indicate that at each time instant in a full-cycle of periodic oscillations in the tube, there exists a switch in the direction of fluctuations in the tube geometry along the length of the tube. That is, in the first stage of switch in oscillations, when the downstream end of the tube experiences a collapse, the tube geometry certain distance upstream of the location of mean collapse exhibits an expansion about its mean position. This may be attributed to a difference in the time scale of advection of fluid inside the tube and the time scale associated with the change in tube geometry. Due to a slower response of the fluid compared to changes in tube dimensions and due to its inertia, there is a pressure build-up upstream of the location of mean collapse. In the next stage of switch in the tube oscillations, when the downstream end of the tube expands during the cycle, the previously accumulated fluid pressure upstream of the collapse is reduced. This causes the upstream regions of the tube to experience a collapse with respect to its mean dimensions. Pressure discharge during this stage is also accompanied by a corresponding increase in flow velocity through the available throttled area. This, in turn, causes a reduction in pressure in the downstream compliant section, which pushes the tube to collapse beyond its mean position. In this manner, the cycle of oscillations repeats.

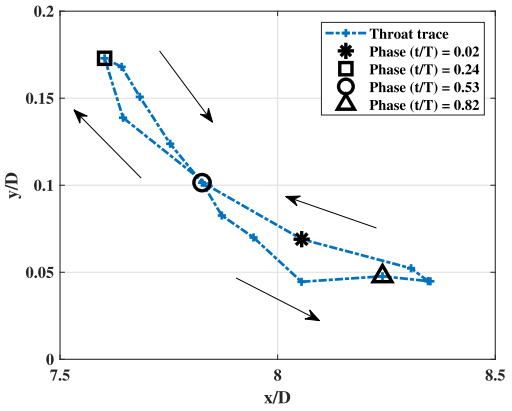

Fig. 12. Trace of the location of the throat/largest constriction within the collapsible tube for Reynolds number $Re_D = 503$. The throat was extracted along a longitudinal slice of the tube, in the z/D = 0 plane. The markers indicate the phases during one cycle of downstream pressure fluctuations seen in Fig. 8(a). The 'asterisk' and 'circle' symbols represent the instants at which minima and maxima are seen in the pressure fluctuations, respectively. Cycle time period, T = 1.143 s.

Furthermore, if we shift our attention to the influence of oscillations in tube geometry on the downstream flow field, Fig. 12 yields interesting observations. The trace of the location of the throat shows that the peak value of downstream pressure lags behind the instant with the largest throat radius by t/T value of 0.19. However, the minima in downstream pressure lags behind the instant with the smallest throat radius by t/T value of 0.12. Here, we recall that fluid advection was identified as the medium for the propagation of disturbances from the tube geometry to the downstream flow field. Essentially, when the tube throat size was the largest over a period of oscillation, the pressure at the throat can also be expected to be the largest. Consequently, the bulk fluid velocity at the throat would also be lower, and the propagation of the disturbance introduced by a reduction in the throat size would also be slower. On the other hand, when the throat area is the smallest over a period of oscillation, any small increase in throat size leads to a sharp increase in velocity. This results in disturbances propagating faster to the downstream flow field. Finally, the variation in the propagation speed of disturbances during the different stages of oscillations may explain the manifestation of the LU-type downstream pressure fluctuations.

The evolution of the cross-sectional area of the tube seen in this study can also be related to the observations made in the numerical studies of Stewart et al. (2010) and Xu and Jensen (2015) on flow through collapsible channels and in the experimental study of Anderson et al. (2016). Numerical studies report that a flexible membrane that constitutes one of the walls in a channel flow can exhibit sloshing or slamming-type oscillations. While sloshing involves high-frequency and low-amplitude tube oscillations that can be observed when the tube is under large tensile force, slamming is known to be characterized by low-frequency vigorous displacements when the tube is under low tension. In this scenario, hydrodynamic modes are expected to contribute to global instabilities (Stewart et al., 2010). The LU-type oscillations observed in the current study can be correlated to the slamming-type oscillations in the tube. Synonymous with the explanation provided by Anderson et al. (2016), the constriction occurs primarily near the downstream end of the tube. With time the collapse gradually increases, and once the largest collapse is achieved, the tube is thrown open over a short time span due to the build-up of pressure upstream of the collapse.

4.2. Relevance to physiological flows

In the previous sections, the geometric features of the collapsible tube and the associated flow features were examined under different regimes from a fundamental standpoint. In this section, physiological implications are examined over a Reynolds number range of $350 \lesssim Re \lesssim 700$, and non-dimensional stiffness range of $0.3 \lesssim \beta \lesssim 1.3$, that were used in this study. These values correspond to conditions pertinent to carotid bifurcation flows (Ku and Giddens, 1983; Ku et al., 1985; Khamdaeng et al., 2012; Limbu et al., 2006; Howard et al., 1993; Skacel and Bursa, 2022), oscillations in collapsible tubes relevant to wheezing (Bertram, 2008; Polio et al., 2019; Hampton et al., 2000; Montaudon et al., 2007; Butler et al., 1986; Reynolds, 1982), and collapse of the internal jugular veins (Holmlund et al., 2017; Vitello et al., 2015; Nakagawa et al., 2016; Skacel and Bursa, 2022; Leguy et al., 2010), among others. When considering cardiovascular applications, these results would be relevant to flows in larger arteries (4 mm $\leq D \leq$ 25 mm, (Ayyaswamy, 2012)) due to the Newtonian nature of the working fluid used in this study.

The shear stresses exerted due to fluid flow on the surfaces (walls) of the arteries and blood vessels are known to play an important role (Ku and Giddens, 1983; Ku et al., 1985). To this end, two important parameters are reported in the literature that are based on wall shear stress. These are Time Averaged Wall Shear Stress (TAWSS) and Oscillatory Shear Index (OSI), as defined in Eqs. (4) and (5), respectively.

$$TAWSS = \frac{1}{T}\left(\int_0^T |\tau_{wall}|\, dt\right) \tag{4}$$

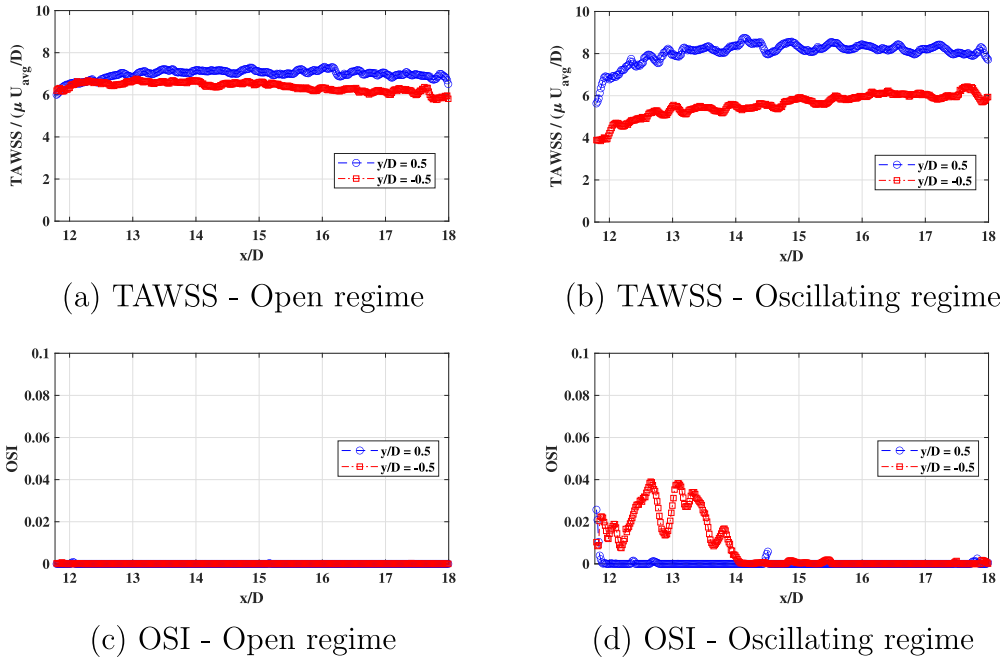

Fig. 13. Variation in Time Averaged Wall Shear Stress (TAWSS) and Oscillatory Shear Index (OSI) on the two walls of PIV domain for a Reynolds number $Re_D = 503$.

$$OSI = \frac{1}{2}\left(1 - \frac{\frac{1}{T}\left|\int_0^T \tau_{wall}\, dt\right|}{TAWSS}\right) \tag{5}$$

Low values of TAWSS and high values of OSI have been reported to have long-term significant consequences depending on the circumstances. For example, these conditions are known to promote plaque deposition in blood vessels and lead to their narrowing, i.e., stenosis (Chi et al., 2018; Owais et al., 2023). On the other hand, in the event of a preexisting enlarged blood vessel such as an aneurysm (Nordon et al., 2011), low TAWSS, and high OSI values are known to promote the growth of abnormalities on the vessel wall that cause rupture in the long term (Mutlu et al., 2023). These observations are reported for periodic flow through blood vessels, caused by the cardiac cycle. However, in the event that self-excited oscillations also exist due to fluid–structure interactions associated with flow through a collapsible tube, both TAWSS and OSI values may play a more crucial role.

To understand these implications, the TAWSS and OSI values are calculated along the two horizontal walls (y/D = −0.5 and 0.5) of the PIV domain. The vector resolution within field of view during PIV measurements was 0.44 mm resulting in a total of 58 vectors across the diameter of the tube. The uncertainty in shear stress measurements is estimated to be within ± 7% of the mean shear stress in the fully-open regime of the tube. The streamwise variations in the TAWSS and OSI parameters, are then plotted for the tube under fully open and oscillating regimes, as shown in Fig. 13. The plots indicate that the TAWSS values are nominally similar across the two walls and constant throughout the tube length, in the fully open regime. Whereas in the oscillating regime, the TAWSS gradually increases and asymptotes to a certain value downstream. These values are relatively higher than the TAWSS in the open regime for y/D = 0.5, but lower at y/D = −0.5. This asymmetry is expected to be introduced by the marginal tilt in the axis of tube collapse with respect to the plane of the PIV domain. In general, OSI values range from 0 to 0.5, with 0 indicating a unidirectional WSS and 0.5 representing oscillatory WSS (Tang et al., 2006; Les et al., 2010). Furthermore, in the context of tracheal flows, OSI has also been recently used by researchers elsewhere as a diagnostic indicator, such as Tiwari et al. (2023). Following this, here the OSI values in the fully open regime are zero throughout the tube wall, due to the absence of any flow field fluctuations, and are indicative of unidirectional flow. However, in the oscillating regime, the OSI values are seen to peak up to 0.04 only on one of the walls. This indicates the presence of a weak recirculation region close to the lower wall (y/D = −0.5) that changes the direction of flow during each cycle. Beyond x/D = 14 (4 diameters from the end of the collapsible tube), the OSI values return to zero.

Although the peak OSI values calculated in the current study are not significantly large enough to correlate with any specific physiological implications, it is expected that, depending on the properties of the fluid and tube stiffness, operating conditions can lead to large-scale fluctuations in flow properties. These may result in conditions of high OSI values. But more importantly, based on operating conditions, one can quantify the span of the downstream section of the tube that is exposed to oscillatory shear stresses, which will ultimately be tied to physiological consequences.

4.3. Limitations and future work

The stereophotogrammetry technique used in this study is associated with certain limitations. First, the speckle-patterned tube surface obstructs the view of the cameras, of its opposite face. This inhibits the tracking of surface deformations in this region. Second, due to this limitation, it is assumed that deformations about the vertical axis of collapse are symmetric. In regions of large collapse ($A/A_{ideal} < 0.5$), this assumption may be inaccurate and the uncertainties in the cross-sectional profiles and areas are marginally higher. Third, the axis along which the tube deforms the largest is generally horizontal and is concurrent with the PIV measurement plane. But in the conditions of large collapse, the axis is slightly tilted away from the horizontal ($\approx 15°$) which translates to an uncertainty of $\leq 3.4\%$ in the velocity. The axis of collapse of the tube being preferentially inclined may be caused by residual strain introduced due to the uncertainty in the tube thickness ($\sim$3% of the tube thickness, t_t) as a result of the tolerance imposed by the 3D-printed mold.

To overcome these limitations and improve the understanding of the mechanisms in collapsible tubes, the following ideas stand to be implemented in the future. Firstly, to overcome the gap in surface measurements due to a lack of visual of the opposite face of the tube, additional cameras can be instrumented to generate a complete azimuthal reconstruction. This will provide a better metric of the uncertainties associated with surface reconstructions performed with only two cameras. Second, volumetric velocity field measurements can be performed to extract the relevant flow field dynamics along planes that are concurrent with either axes of tube collapse, which will provide a more accurate quantification of the wall shear stress parameters. Finally, while this study focuses chiefly on a limited set of operating conditions in each regime, a more detailed characterization of the tube dynamics is expected to be performed over a well-resolved parameter set. This will help to provide a better understanding of the three-dimensionality of tube fluctuations and their relationship to the flow field.

5. Conclusions

One of the key objectives of this study was to examine the relationship between flow and geometric features in a collapsible tube. This was enabled by simultaneously characterizing the three-dimensional structural deformations of the tube using the stereo-photogrammetry technique and the flow field downstream of the tube using pressure measurements and planar particle image velocimetry. In the first stage, the response of the tube was qualitatively mapped over a range of operating conditions. This helped in identifying the operating conditions that correspond to the distinct operational regimes, viz. fully open, fully closed, and oscillating. At specific conditions corresponding to each of these regimes, time-synchronized measurements of flow rate, upstream and downstream pressures, stereophotogrammetry, and planar PIV were performed.

The results suggested that, under the fully open regime, the tube exhibits a uniform and ideal circular cross-sectional profile and constant area throughout the length of the tube. In the absence of any deformations, the pressure loss across the ends of the tube and the velocity field downstream of the tube were indicative of a fully developed laminar flow profile (Hagen–Poiseuille flow). In the collapsed regime, the tube achieved the largest collapse closer to the far downstream end with a dumbbell profile while gradually transitioning from circular to elliptical shapes. Furthermore, the tube throttled the flow at the location of the largest collapse, which, in turn, translated to a reduced velocity in the downstream pipe compared to the fully open regime.

Under intermediate operating conditions, the tube exhibited self-sustained limit-cycle oscillations which manifested in the form of variations in tube geometry with respect to its time-averaged position, LU-type fluctuations in downstream pressure, and a dynamic velocity field. The fluctuations in the geometric and flow field properties were found to be dictated globally by a single dominant mode. Although fluctuations along the minor axis of collapse of the tube were oppositely correlated with those along the major axis, they also primarily dictated any flow field variations due to a larger amplitude of fluctuations. Furthermore, a large section of the tube downstream of the largest collapse experienced fully coherent oscillations that are in phase. Upstream of this region, a switch in the direction of tube oscillations was observed. Any contraction of the tube in the downstream region caused the accumulation of fluid and build-up of pressure upstream of the largest collapse, which in turn caused the tube in these sections to expand. During the expansion phase of the downstream sections of the tube, the upstream sections collapsed. The fluctuations in the downstream flow field were found to be influenced by the propagation of disturbances due to oscillations in tube geometry, through the advection of fluid through the tube. Furthermore, the manifestation of the LU-type pressure fluctuations was found to be due to the variation in the propagation speed of the disturbances during the different stages within a period of oscillation of the tube.

Finally, the wall shear stress measurements in the sections downstream of the collapsible tube showed that there was an increase in the time-averaged wall shear stress and oscillatory shear index on at least one of the walls in the oscillating regime compared to the fully open regime, while one of the walls had a reduction in time-averaged shear stress. Although these changes were not significant under the operating conditions tested, they were expected to have implications in cardiovascular flows when the conditions were not suitable.

CRediT authorship contribution statement

Vikas N. Bhargav: Writing – review & editing, Writing – original draft, Visualization, Validation, Methodology, Investigation, Formal analysis, Data curation. **Nicola Francescato:** Writing – review & editing, Visualization, Validation, Methodology, Data curation. **Holger Mettelsiefen:** Writing – review & editing, Visualization, Methodology, Formal analysis. **Abdullah Y. Usmani:** Writing – review & editing, Visualization, Validation. **Stefania Scarsoglio:** Writing – review & editing, Supervision, Project administration. **Vrishank Raghav:** Writing – review & editing, Supervision, Methodology, Funding acquisition, Conceptualization.

Declaration of competing interest

The authors declare that they have no known competing financial interests or personal relationships that could have appeared to influence the work reported in this paper.

Data availability

Data will be made available on request.

Acknowledgments

This research was funded by the National Institutes of Health (NIH) Grant Number -R21EB027891 and partially supported by the National Science Foundation (NSF) Grant Number CBET – 2145189 . The authors also acknowledge the assistance of members of the Applied Fluid Research Group, Dr. Eldon Triggs, and Mr. Andy Weldon in the Department of Aerospace Engineering at Auburn University.

Appendix A. Supplementary data

Supplementary material related to this article can be found online at https://doi.org/10.1016/j.jfluidstructs.2024.104122.

References

Amin, M.Z.F., Garman, K., Rhee, J.S., Woodson, B.T., Garcia, G.J., 2021. Effect of tube length on the buckling pressure of collapsible tubes. Comput. Biol. Med. 136, 104693.

Anderson, P., Fels, S., Green, S., 2016. Experimental characterization of the oscillatory behavior of a quasi-two-dimensional collapsible channel. J. Fluids Struct. 66, 254–268. http://dx.doi.org/10.1016/j.jfluidstructs.2016.07.009.

Ayyaswamy, P.S., 2012. Chapter 16 - Introduction to biofluid mechanics. In: Kundu, P.K., Cohen, I.M., Dowling, D.R. (Eds.), Fluid Mechanics (Fifth Edition), Fifth Edition Academic Press, Boston, pp. 779–852. http://dx.doi.org/10.1016/B978-0-12-382100-3.10016-2.

Bai, Z., Zhu, L., 2019. Simulation of blood flow past a distal arteriovenous-graft anastomosis at low Reynolds numbers. Phys. Fluids 31 (9), 091902. http://dx.doi.org/10.1063/1.5099635.

Bertram, C.D., 2008. Flow-induced oscillation of collapsed tubes and airway structures. Respir. Physiol. Neurobiol. 163 (1), 256–265. http://dx.doi.org/10.1016/j.resp.2008.04.011, Respiratory Biomechanics.

Bertram, C., Elliott, N., 2003. Flow-rate limitation in a uniform thin-walled collapsible tube, with comparison to a uniform thick-walled tube and a tube of tapering thickness. J. Fluids Struct. 17 (4), 541–559. http://dx.doi.org/10.1016/S0889-9746(02)00160-3.

Bertram, C.D., Nugent, A.H., 2005. The flow field downstream of an oscillating collapsed tube. J. Biomech. Eng. 127 (1), 39–45. http://dx.doi.org/10.1115/1.1835351.

Bertram, C., Pedley, T., 1982. A mathematical model of unsteady collapsible tube behaviour. J. Biomech. 15 (1), 39–50. http://dx.doi.org/10.1016/0021-9290(82)90033-1.

Bertram, C.D., Raymond, C.J., Butcher, K.S.A., 1989. Oscillations in a collapsed-tube analog of the brachial artery under a sphygmomanometer cuff. J. Biomech. Eng. 111 (3), 185–191. http://dx.doi.org/10.1115/1.3168364.

Bertram, C., Raymond, C., Pedley, T., 1990. Mapping of instabilities for flow through collapsed tubes of differing length. J. Fluids Struct. 4 (2), 125–153. http://dx.doi.org/10.1016/0889-9746(90)90058-D.

Bertram, C.D., Truong, N.K., Hall, S.D., 2008. PIV measurements of the flow field just downstream of an oscillating collapsible tube. J. Biomech. Eng. 130 (6), 061011. http://dx.doi.org/10.1115/1.2985071.

Bertram, C., Tscherry, J., 2006. The onset of flow-rate limitation and flow-induced oscillations in collapsible tubes. J. Fluids Struct. 22 (8), 1029–1045. http://dx.doi.org/10.1016/j.jfluidstructs.2006.07.005.

Butler, J.P., Nakamura, M., Sasaki, H., Sasaki, T., Takishima, T., 1986. Poissons' ratio of lung parenchyma and parenchymal interaction with bronchi. Jpn. J. Physiol. 36 (1), 91–106. http://dx.doi.org/10.2170/jjphysiol.36.91.

Cancelli, C., Pedley, T.J., 1985. A separated-flow model for collapsible-tube oscillations. J. Fluid Mech. 157, 375–404. http://dx.doi.org/10.1017/S0022112085002427.

Chi, Z., Seo, J.H., Mittal, R., 2018. Computational modelling and analysis of haemodynamics in a simple model of aortic stenosis. J. Fluid Mech. 851, 23–49.

Conrad, W.A., 1969. Pressure–flow relationships in collapsible tubes. IEEE Trans. Bio-Med. Eng. 16 (4), 284–295. http://dx.doi.org/10.1109/tbme.1969.4502660.

Dai, G., Gertler, J.P., Kamm, R.D., 1999. The effects of external compression on venous blood flow and tissue deformation in the lower leg. J. Biomech. Eng. 121 (6), 557–564. http://dx.doi.org/10.1115/1.2800853.

Grotberg, J.B., Jensen, O.E., 2004. Biofluid mechanics in flexible tubes. Annu. Rev. Fluid Mech. 36 (1), 121–147. http://dx.doi.org/10.1146/annurev.fluid.36.050802.121918.

Hampton, T., Armstrong, S., Russell, W.J., 2000. Estimating the diameter of the left main bronchus. Anaesth. Intensive Care 28 (5), 540–542. http://dx.doi.org/10.1177/0310057X0002800510, PMID: 11094671.

Hazel, A.L., Heil, M., 2003. Steady finite-Reynolds-number flows in three-dimensional collapsible tubes. J. Fluid Mech. 486, 79–103. http://dx.doi.org/10.1017/S0022112003004671.

Heil, M., Boyle, J., 2010. Self-excited oscillations in three-dimensional collapsible tubes: Simulating their onset and large-amplitude oscillations. J. Fluid Mech. 652, 405–426. http://dx.doi.org/10.1017/S0022112010000157.

Heil, M., Hazel, A.L., 2011. Fluid-structure interaction in internal physiological flows. Annu. Rev. Fluid Mech. 43 (1), 141–162. http://dx.doi.org/10.1146/annurev-fluid-122109-160703.

Heil, M., Waters, S.L., 2006. Transverse flows in rapidly oscillating elastic cylindrical shells. J. Fluid Mech. 547, 185–214. http://dx.doi.org/10.1017/S0022112005007214.

Holmlund, P., Johansson, E., Qvarlander, S., Wåhlin, A., Ambarki, K., Koskinen, L.O.D., Malm, J., Eklund, A., 2017. Human jugular vein collapse in the upright posture: Implications for postural intracranial pressure regulation. Fluids Barriers CNS 14 (1), 2045–8118. http://dx.doi.org/10.1186/s12987-017-0065-2.

Howard, G., Sharrett, A.R., Heiss, G., Evans, G.W., Chambless, L.E., Riley, W.A., Burke, G.L., 1993. Carotid artery intimal-medial thickness distribution in general populations as evaluated by B-mode ultrasound. ARIC Investig.. Stroke 24 (9), URL https://pubmed.ncbi.nlm.nih.gov/8362421.

Jensen, O.E., 1990. Instabilities of flow in a collapsed tube. J. Fluid Mech. 220, 623–659. http://dx.doi.org/10.1017/S0022112090003408.
Jensen, O.E., Heil, M., 2003. High-frequency self-excited oscillations in a collapsible-channel flow. J. Fluid Mech. 481, 235–268. http://dx.doi.org/10.1017/S002211200300394X.
Katz, A.I., Chen, Y., Moreno, A.H., 1969. Flow through a collapsible tube. Experimental analysis and mathematical model. Biophys. J. 9 (104), 1261–1279. http://dx.doi.org/10.1016/S0006-3495(69)86451-9.
Khamdaeng, T., Luo, J., Vappou, J., Terdtoon, P., Konofagou, E., 2012. Arterial stiffness identification of the human carotid artery using the stress-strain relationship in vivo. Ultrasonics. Ultrasonics 52 (3), http://dx.doi.org/10.1016/j.ultras.2011.09.006.
Knowlton, F.P., Starling, E.H., 1912. The influence of variations in temperature and blood-pressure on the performance of the isolated mammalian heart. J. Physiol. 44 (3), 206–219. http://dx.doi.org/10.1113/jphysiol.1912.sp001511.
Ku, D.N., Giddens, D.P., 1983. Pulsatile flow in a model carotid bifurcation. Arteriosclerosis: Off. J. Am. Heart Assoc., Inc. 3 (1), 31–39. http://dx.doi.org/10.1161/01.ATV.3.1.31, URL https://www.ahajournals.org/doi/abs/10.1161/01.ATV.3.1.31.
Ku, D.N., Giddens, D.P., Zarins, C.K., Glagov, S., 1985. Pulsatile flow and atherosclerosis in the human carotid bifurcation. Positive correlation between plaque location and low oscillating shear stress. Arteriosclerosis: Off. J. Am. Heart Assoc., Inc. 5 (3), 293–302. http://dx.doi.org/10.1161/01.ATV.5.3.293, URL https://www.ahajournals.org/doi/abs/10.1161/01.ATV.5.3.293.
Kumar, K., Prabhakaran, D., 2022. Nonlinear oscillations of a collapsible tube subjected to unsteady external pressure. Phys. Fluids 34 (6), 061907. http://dx.doi.org/10.1063/5.0092737.
Leguy, C., Bosboom, E., Gelderblom, H., Hoeks, A., van de Vosse, F., 2010. Estimation of distributed arterial mechanical properties using a wave propagation model in a reverse way. Med. Eng. Phys. 32 (9), 957–967. http://dx.doi.org/10.1016/j.medengphy.2010.06.010.
Les, A.S., Shadden, S.C., Figueroa, C.A., Park, J.M., Tedesco, M.M., Herfkens, R.J., Dalman, R.L., Taylor, C.A., 2010. Quantification of hemodynamics in abdominal aortic aneurysms during rest and exercise using magnetic resonance imaging and computational fluid dynamics. Ann. Biomed. Eng. 38 (4), 1288–1313. http://dx.doi.org/10.1007/s10439-010-9949-x.
Limbu, Y., Gurung, G., Malla, R., Rajbhandari, R., Regmi, S., 2006. Assessment of carotid artery dimensions by ultrasound in non-smoker healthy adults of both sexes. Nepal Med. College J. 8 (3), URL https://pubmed.ncbi.nlm.nih.gov/17203830.
Liu, H.F., Luo, X.Y., Cai, Z.X., Pedley, T.J., 2009. Sensitivity of unsteady collapsible channel flows to modelling assumptions. Commun. Numer. Methods. Eng. 25 (5), 483–504. http://dx.doi.org/10.1002/cnm.1217.
Luo, X., Pedley, T., 1995. A numerical simulation of steady flow in a 2-D collapsible channel. J. Fluids Struct. 9 (2), 149–174. http://dx.doi.org/10.1006/jfls.1995.1008.
Luo, X.Y., Pedley, T.J., 1996. A numerical simulation of unsteady flow in a two-dimensional collapsible channel. J. Fluid Mech. 314, 191–225. http://dx.doi.org/10.1017/S0022112096000286.
Luo, X.Y., Pedley, T., 1998. The effects of wall inertia on flow in a two-dimensional collapsible channel. J. Fluid Mech. 363, 253–280. http://dx.doi.org/10.1017/S0022112098001062.
Luo, X.Y., Pedley, T.J., 2000. Multiple solutions and flow limitation in collapsible channel flows. J. Fluid Mech. 420, 301–324. http://dx.doi.org/10.1017/S002211200000152X.
Marzo, A., Luo, X., Bertram, C., 2005. Three-dimensional collapse and steady flow in thick-walled flexible tubes. J. Fluids Struct. 20 (6), 817–835. http://dx.doi.org/10.1016/j.jfluidstructs.2005.03.008, Axial-Flow Fluid-Structure Interactions.
Montaudon, M., Desbarats, P., Berger, P., Dietrich, G.D., Marthan, R., Laurent, F., 2007. Assessment of bronchial wall thickness and lumen diameter in human adults using multi-detector computed tomography: Comparison with theoretical models. J. Anatomy 211 (5), 579–588. http://dx.doi.org/10.1111/j.1469-7580.2007.00811.x.
Mutlu, O., Salman, H.E., Al-Thani, H., El-Menyar, A., Qidwai, U.A., Yalcin, H.C., 2023. How does hemodynamics affect rupture tissue mechanics in abdominal aortic aneurysm: Focus on wall shear stress derived parameters, time-averaged wall shear stress, oscillatory shear index, endothelial cell activation potential, and relative residence time. Comput. Biol. Med. 154, 106609. http://dx.doi.org/10.1016/j.compbiomed.2023.106609.
Nahar, S., Dubey, B.N., Windhab, E.J., 2019. Influence of flowing fluid property through an elastic tube on various deformations along the tube length. Phys. Fluids 31 (10), 101905. http://dx.doi.org/10.1063/1.5123182.
Nakagawa, D., Shojima, M., Yoshino, M., Kin, T., Imai, H., Nomura, S., Saito, T., Nakatomi, H., Nakatomi, H., Saito, N., 2016. Wall-to-lumen ratio of intracranial arteries measured by indocyanine green angiography. Asian J. Neurosurg. 11, 361–364. http://dx.doi.org/10.4103/1793-5482.175637.
Nordon, I.M., Hinchliffe, R.J., Loftus, I.M., Thompson, M.M., 2011. Pathophysiology and epidemiology of abdominal aortic aneurysms. Nat. Rev. Cardiol. 8 (2), 92–102. http://dx.doi.org/10.1038/nrcardio.2010.180.
Owais, M., Usmani, A.Y., Muralidhar, K., 2023. Effect of a bend on vortex formation and evolution in a three-dimensional stenosed geometry during pulsatile flow. Phys. Fluids 35 (3), 031906. http://dx.doi.org/10.1063/5.0138825.
Pedley, T., 1992. Longitudinal tension variation in collapsible channels: A new mechanism for the breakdown of steady flow. ASME. J Biomech. Eng. 114, 60–67. http://dx.doi.org/10.1115/1.2895451.
Podoprosvetova, A., Zayko, J., Yushutin, V., Vedeneev, V., 2021. Experimental study of the flow regime effect on the stability of collapsible tubes conveying fluid. Phys. Fluids 33 (6), 064104. http://dx.doi.org/10.1063/5.0050745.
Polio, S.R., Stasiak, S.E., Jamieson, R.R., Balestrini, J.L., Krishnan, R., Parameswaran, H., 2019. Extracellular matrix stiffness regulates human airway smooth muscle contraction by altering the cell-cell coupling. Sci. Rep. 9 (1), 2045–2322. http://dx.doi.org/10.1038/s41598-019-45716-9.
Reynolds, D.B., 1982. Steady expiratory flow-pressure relationship in a model of the human bronchial tree. J. Biomech. Eng. 104 (2), 153–158. http://dx.doi.org/10.1115/1.3138330.
Sen, Z., Luo, X., Cai, Z., 2018. Three-dimensional flows in a hyperelastic vessel under external pressure. Biomech. Model. Mechanobiol. 17, 1187–1207.
Shapiro, A.H., 1977. Steady flow in collapsible tubes. J. Biomech. Eng. 99 (3), 126–147. http://dx.doi.org/10.1115/1.3426281.
Skacel, P., Bursa, J., 2022. Poisson's ratio and compressibility of arterial wall – Improved experimental data reject auxetic behaviour. J. Mech. Behav. Biomed. Mater. 131, 105229. http://dx.doi.org/10.1016/j.jmbbm.2022.105229.
Stelios, S., Qin, S., Shan, F., Mathioulakis, D., 2019. Forced and unforced flow through compliant tubes. Meccanica 54 (6), 101905. http://dx.doi.org/10.1007/s11012-019-01002-6.
Stewart, P.S., Heil, M., Waters, S.L., Jensen, O.E., 2010. Sloshing and slamming oscillations in a collapsible channel flow. J. Fluid Mech. 662, 288–319. http://dx.doi.org/10.1017/S0022112010003277.
Tang, B.T., Cheng, C.P., Draney, M.T., Wilson, N.M., Tsao, P.S., Herfkens, R.J., Taylor, C.A., 2006. Abdominal aortic hemodynamics in young healthy adults at rest and during lower limb exercise: Quantification using image-based computer modeling. Am. J. Physiol.-Heart Circul. Physiol. 291 (2), H668–H676. http://dx.doi.org/10.1152/ajpheart.01301.2005, PMID: 16603687.
Tang, C., Zhu, L., Akingba, G., Lu, X.Y., 2015. Viscous flow past a collapsible channel as a model for self-excited oscillation of blood vessels. J. Biomech. 48 (10), 1922–1929. http://dx.doi.org/10.1016/j.jbiomech.2015.04.011.
Tiwari, B., Usmani, A.Y., Bodduluri, S., Bhatt, S.P., Raghav, V., 2023. Influence of pulsatility and inflow waveforms on tracheal airflow dynamics in healthy older adults. J. Biomech. Eng. 145 (10), 101009. http://dx.doi.org/10.1115/1.4062851.
Truong, N.K., Bertram, C.D., 2009. The flow-field downstream of a collapsible tube during oscillation onset. Commun. Numer. Methods. Eng. 25 (5), 405–428. http://dx.doi.org/10.1002/cnm.1226, URL https://onlinelibrary.wiley.com/doi/abs/10.1002/cnm.1226.

Vitello, D., Ripper, R., Fettiplace, M., Weinberg, G., Vitello, J., 2015. Blood density is nearly equal to water density: A validation study of the gravimetric method of measuring intraoperative blood loss. J. Vet. Med. 2356–7708. http://dx.doi.org/10.1155/2015/152730, URL https://www.ncbi.nlm.nih.gov/pmc/articles/PMC4590883/.

Wang, J.W., Chew, Y.T., Low, H.T., 2009. Effects of downstream system on self-excited oscillations in collapsible tubes. Commun. Numer. Methods. Eng. 25 (5), 429–445. http://dx.doi.org/10.1002/cnm.1238.

Wu, H.J., Jia, L.B., Yin, X.Z., 2015. Experiments on self-excited oscillation in a thin-walled collapsible tube. Exp. Self-Excit. Oscil. Thin-Walled Collapsible Tube 31 (6), 817–826. http://dx.doi.org/10.1007/s10409-015-0465-y.

Xu, F., Jensen, O.E., 2015. A low-order model for slamming in a flexible-channel flow. Quart. J. Mech. Appl. Math. 68 (3), 299–319. http://dx.doi.org/10.1093/qjmam/hbv009.

Yiasemides, D., Argyris, A., Mathioulakis, D.S., 2017. Transitory and periodic flow in a self-oscillating collapsible tube: Experimental study. J. Energy Eng. 143 (4), 04017001. http://dx.doi.org/10.1061/(ASCE)EY.1943-7897.0000427, URL https://ascelibrary.org/doi/abs/10.1061/%28ASCE%29EY.1943-7897.0000427.